Available online at www.sciencedirect.com
SCIENCE DIRECT®
Journal of Power Sources 152 (2005) 105–121
JOURNAL OF POWER SOURCES
www.elsevier.com/locate/jpowsour

# Dimensionless numbers and correlating equations for the analysis of the membrane-gas diffusion electrode assembly in polymer electrolyte fuel cells

E.L. Gyenge*

*Department of Chemical and Biological Engineering, The University of British Columbia, 2216 Main Mall, Vancouver, BC, Canada V6T 1Z4*

Received 14 January 2005; accepted 2 February 2005
Available online 13 April 2005

**Abstract**

The Quraishi–Fahidy method [Can. J. Chem. Eng. 59 (1981) 563] was employed to derive characteristic dimensionless numbers for the membrane-electrolyte, cathode catalyst layer and gas diffuser, respectively, based on the model presented by Bernardi and Verbrugge for polymer electrolyte fuel cells [AIChE J. 37 (1991) 1151]. Monomial correlations among dimensionless numbers were developed and tested against experimental and mathematical modeling results. Dimensionless numbers comparing the bulk and surface-convective ionic conductivities, the electric and viscous forces and the current density and the fixed surface charges, were employed to describe the membrane ohmic drop and its non-linear dependence on current density due to membrane dehydration. The analysis of the catalyst layer yielded electrode kinetic equivalents of the second Damköhler number and Thiele modulus, influencing the penetration depth of the oxygen reduction front based on the pseudohomogeneous film model. The correlating equations for the catalyst layer could describe in a general analytical form, all the possible electrode polarization scenarios such as electrode kinetic control coupled or not with ionic and/or oxygen mass transport limitation. For the gas diffusion-backing layer correlations are presented in terms of the Nusselt number for mass transfer in electrochemical systems. The dimensionless number-based correlating equations for the membrane electrode assembly (MEA) could provide a practical approach to quantify single-cell polarization results obtained under a variety of experimental conditions and to implement them in models of the fuel cell stack.


*Keywords:* Polymer electrolyte fuel cells; Gas diffusion electrodes; Dimensionless numbers

## 1. Introduction

It has been forecasted that polymer electrolyte fuel cells (PEFC) could reach widespread commercialization over the next one or two decades as low emission power sources for a variety of applications ranging from electronic devices to transportation. The large-scale commercialization of fuel cells hinges on both socio-economic 'pull' and technology 'push'. Both factors are strongly dependent on the performance–cost relationship. Mathematical modeling has been an integral part of fuel cell research and development, initially at the membrane-gas diffusion electrode assembly (MEA) level (coupled or not with transport phenomena in the flow channels) [1–12], followed up by attempts to develop stack models with varying degree of completeness [13–16].

It is beyond the objective of this section to give a comprehensive review of these models. However, it must be noted that the modeling effort coupled with experimental validation provided a fairly good phenomenological understanding of the physico-chemical and transport phenomena occurring at the MEA level and the projected impact on single-cell performance. The mechanistic understanding of ion and water transport in the polymer membrane-electrolyte together with first-principle-based analysis and the practical application of these models for membrane performance predictions in oper-

* Tel.: +1 604 822 3217; fax: +1 604 822 6003.
*E-mail address:* egyenge@chml.ubc.ca.

0378-7753/$ – see front matter © 2005 Elsevier B.V. All rights reserved.
doi:10.1016/j.jpowsour.2005.02.034

**Nomenclature**

| | |
|---|---|
| $a_c$ | specific surface area of the catalyst layer ($m^2\,m^{-3}$) |
| AC | acid capacity of the membrane ($eq\,kg^{-1}$) |
| $b$ | Tafel slope for $O_2$ reduction ($V\,dec^{-1}$) |
| BW | membrane basis weight ($kg\,m^{-2}$) |
| $C_b$ | bulk concentration ($mol\,m^{-3}$) |
| $C_f$ | fixed charge-site concentration of the membrane ($mol\,m^{-3}$) |
| $D_{A–B}$ | binary gas diffusion coefficient ($m^2\,s^{-1}$) |
| $D_{H^+}$ | $H^+$ diffusion coefficient in the bulk membrane-electrolyte ($m^2\,s^{-1}$) |
| $D_{O_2}$ | dissolved $O_2$ diffusion coefficient in the bulk membrane-electrolyte ($m^2\,s^{-1}$) |
| $D_{O_2,c}$ | effective dissolved $O_2$ diffusion coefficient in the membrane-electrolyte phase of the catalyst layer ($m^2\,s^{-1}$) |
| $Da_{II}$ | the second Damköhler number (electrochemical definition) |
| $E_{oc}$ | open-circuit cell voltage (V) |
| $E^0$ | standard potential for $O_2$ reduction (V versus SHE) |
| EW | membrane equivalent weight ($kg\,eq^{-1}$) |
| $f$ | electrochemical factor ($=\alpha F/RT$) ($V^{-1}$) |
| $F$ | Faraday's constant ($=96{,}487\,C\,mol_{electron}^{-1}$ or $C\,eq^{-1}$) |
| $H$ | Henry's constant ($Pa\,m^3\,mol^{-1}$) |
| $i$ | superficial current density in the membrane-electrolyte phase ($A\,m^{-2}$) |
| $i_L$ | mass transfer limiting superficial current density ($A\,m^{-2}$) |
| $i_s$ | superficial current density in the solid phase ($A\,m^{-2}$) |
| $i_t$ | total (operating) superficial current density ($A\,m^{-2}$) |
| $k_p$ | membrane hydraulic permeability ($m^2$) |
| $k_\Phi$ | electrokinetic permeability ($m^2$) |
| $k^0$ | standard heterogeneous rate constant ($m\,s^{-1}$) |
| $l$ | characteristic length (m) |
| $\frac{n}{s_j}$ | number of moles of electrons per mole of species $j$ ($mol_{electron}\,mol^{-1}$) |
| $N_d$ | number of dimensionless groups |
| $N_{SI}$ | number of SI units |
| $Nu_E$ | mass transfer Nusselt number (electrochemical definition) |
| $p_d$ | inlet air pressure in the diffuser ($N\,m^{-2}$) |
| $\Delta p$ | hydraulic pressure difference ($N\,m^{-2}$) |
| $q_f$ | fixed-negative surface charge density ($C\,m^{-2}$) |
| $r_p$ | membrane pore radius (m) |
| $R$ | universal gas constant ($J\,mol^{-1}\,K^{-1}$) |
| $Re$ | Reynolds number |
| $s_j$ | stoichiometric coefficient of species $j$ (either $H^+$ or $O_2$) |
| $Sh$ | Sherwood number |
| $T$ | temperature (K) |
| $u$ | ionic mobility ($m^2\,s^{-1}\,V^{-1}$) |
| $v_0$ | superficial water velocity ($m\,s^{-1}$) |
| $Wa$ | Wagner number |
| $x$ | gas mole fraction |
| $y$ | exponents and/or constants in the correlating functions |
| $z_f$ | charge number for the fixed sites of the proton exchange membrane ($=-1$) |
| $Z$ | position along the MEA thickness |
| $Z_c$ | catalyst layer thickness (m) |
| $Z_d$ | diffuser thickness (m) |
| $Z_m$ | 'wet' membrane thickness (m) |

*Greek symbols*

| | |
|---|---|
| $\alpha$ | transfer coefficient for $O_2$ reduction |
| $\gamma_w$ | water activity coefficient |
| $\eta$ | overpotential for $O_2$ reduction (V) |
| $\theta_m$ | membrane water uptake ($m^3\,m^{-3}$) |
| $\kappa$ | membrane-electrolyte specific conductivity ($S\,m^{-1}$) |
| $\kappa_0$ | membrane-electrolyte specific conductivity at zero current (i.e. open-circuit conditions) ($S\,m^{-1}$) |
| $\lambda$ | membrane water content (i.e. number of water molecules per fixed ionic group) |
| $\mu$ | dynamic viscosity (Pa s) |
| $\nu_p$ | reaction front penetration depth inside the catalyst layer (m) |
| $\pi$ | dimensionless number |
| $\rho$ | density ($kg\,m^{-3}$) |
| $\sigma$ | electronic conductivity of the solid-matrix phase ($S\,m^{-1}$) |
| $\tau$ | slope of the $\phi_E$ versus $\pi_{10}$ dependence |
| $\phi$ | Thiele modulus |
| $\Phi$ | the potential in the ionic conductor polymer electrolyte phase (V) |
| $\Phi_s$ | the potential in the solid, electronic conductor, phase (V) |
| $\Psi$ | correlating function |

*Subscripts*

| | |
|---|---|
| c | catalyst layer (it also refers to effective values of parameters in the porous catalyst layer) |
| d | gas diffusion layer (it also refers to effective values of parameters in the porous gas-diffusion layer) |
| E | related to electrodes and electrochemical systems |
| f | fixed-negative charges on the membrane |
| l | limiting value for linear dependence of the membrane ohmic drop versus current density |
| L | mass transfer limiting |

| | |
|---|---|
| m | proton exchange membrane (polymer electrolyte) |
| s | solid-matrix electronic conductor phase |
| t | total (i.e. electronic and ionic conductor phases) |
| w | water phase |
| 0 | inlet to the gas-diffusion layer |
| 1 | catalyst/gas-diffusion layer interface |
| 2 | bulk membrane-electrolyte/catalyst layer interface |

ating fuel cells, is less developed and it is a subject of intense research (for a review see [17]).

With the fuel cell development effort focusing increasingly on stack engineering and optimization, there is a need, as noted also by Appleby and co-workers [13], for comprehensive yet numerically less extensive equations descriptive of the MEA performance in order to be easily implemented into complex numerical models of the fuel cell stack. Therefore, in parallel with phenomenological and mechanistic models, empirical equations have been developed to describe the fuel cell voltage $E$ as a function of current density $i$. The equation proposed by Chamberlain and co-workers (Eq. (1)) showed good fit with experimentally measured data [18]:

$$E = E_{oc} - b\log i - Ri - \gamma\exp(\omega i), \quad (1)$$

where $b$ is the Tafel slope for oxygen reduction ($V\,dec^{-1}$), $E$ and $E_{oc}$ the operating and open-circuit cell voltages, respectively (V), $i$ the superficial current density ($A\,m^{-2}$), $R$ the area-specific ohmic resistance of the membrane ($\Omega\,m^2$), $\gamma$ (V) and $\omega$ ($m^2\,A^{-1}$) the empirical curve fitting parameters.

The exponential term in Eq. (1) expresses empirically the mass transfer limitation of the polarization curve [18]. Moreover, the coefficient $b$ in Eq. (1) is often used as an additional curve fitting parameter.

Amphlett et al. developed an empirical model as well, to fit the experimentally obtained polarization curves of a Ballard fuel cell [19]. The features of their cell voltage model were: linear dependence of the internal resistance on current density and temperature, and logarithmic dependence of the overpotential on both current density (i.e. Tafel regime) and effective oxygen concentration coupled with a linear temperature function correlated by respective parametric coefficients.

While the proposed empirical equations are successful in describing the overall single-cell polarization there is an inherent lack of transparency associated with them, which could restrict the applicability to the specific conditions and possibly cell designs used in determining the empirical parameters.

The goal of the present investigation was to determine characteristic dimensionless numbers for each component of the MEA (exemplified on the cathode side, Fig. 1) and furthermore, to evaluate whether monomial correlations among dimensionless ratios could be derived to provide, after testing against experimental data, easy to use equations linking essential physico-chemical properties with fuel cell operating parameters.

Dimensional analysis, although a time-honored technique (for a recent review see the monograph by Szirtes [20]), as a stand-alone modeling method for chemical engineering is typically limited to simple cases of transport processes where a list of variables could be straightforwardly compiled. This approach is clearly not applicable to more complex systems especially those involving both transport phenomena and chemical/electrochemical reactions. However, as noted by Churchill, dimensional analysis applied to a mathematical model of the system, eliminates the uncertainty associated with the selection of variables and useful quantitative results in the form of dimensionless correlations could be obtained. In those cases the dimensional analysis results could describe the system to the extent of the mathematical model they are based upon [21].

In a review of dimensional analysis applications for electrochemical reactors, Selman also concluded that due to the large number of interacting variables, 'blind' dimensional analysis must be avoided and dimensional analysis could only be useful when coupled with a mathematical model of the system [22]. In the present work the dimensional analysis procedure developed by Quraishi and Fahidy [23] was applied to the variables, parameters and constants encountered in the one-dimensional MEA model presented by Bernardi and Verbrugge [4,5]. Furthermore, monomial correlating functions among dimensionless numbers are proposed and tested against experimental data and mathematical modeling results from the literature.

## 2. Model summary of the membrane-gas diffusion electrode assembly

Fig. 1 shows schematically the three components of the MEA, gas diffusion layer, catalyst layer (i.e. reaction zone) and the membrane-electrolyte. Here the MEA is described in relation to the cathode reaction:

$$O_2 + 4H^+ + 4e^- \Leftrightarrow 2H_2O,$$
$$E^0 = 1.23\,V_{SHE}\ \text{at}\ 298\,K. \quad (2)$$

The Bernardi–Verbrugge model, selected as basis for the dimensionless analysis, has been discussed extensively in the literature and compared to experimental results [4,5]. It is essentially based on the macroscopic, volume averaged, porous electrode model [24], coupled on the membrane side with the dilute electrolyte assumption for ion transport and Schlögl's equation for water transport, whilst the Stefan–Maxwell equation and material balance equations are employed to describe the gas diffuser. Ohm's law, written in terms of effective conductivities, is applied to describe the

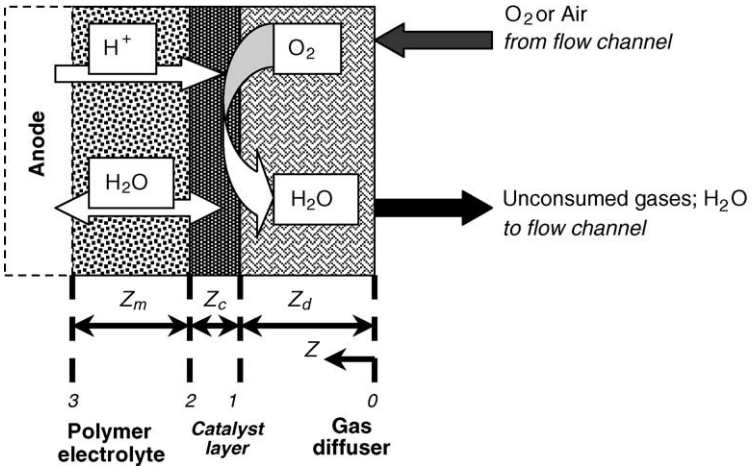


Fig. 1. Schematic representation of the membrane-gas diffusion electrode assembly (MEA) on the cathode side of the polymer electrolyte fuel cell.

potential drop in the electronic and ionic conductive phases of the porous electrode as a function of current density.

The transfer current per unit electrode volume between the solid-matrix and polymer electrolyte phases for the cathodic direction of oxygen reduction (Eq. (2)), considering first-order kinetics with respect to dissolved oxygen concentration and the proton concentration effect factored in the rate constant, is given by

$$\frac{\mathrm{d}i}{\mathrm{d}Z} = \frac{n}{s_{\mathrm{O_2}}} F a_{\mathrm{c}} k^0 C_{\mathrm{O_2}} \exp(-f(\Phi_{\mathrm{s}} - \Phi - E^0)) = a_{\mathrm{c}} i_0 \left(\frac{C_{\mathrm{O_2}}}{C_{\mathrm{O_2,ref}}}\right) \exp(-f(\Phi_{\mathrm{s}} - \Phi - E^0)), \quad (3)$$

where $f = \frac{\alpha F}{RT}$, $a_{\mathrm{c}}$ the specific surface area of the catalyst layer, $C_{\mathrm{O_2}}$ the actual dissolved $O_2$ concentration in the polymer electrolyte phase of the catalyst layer, $C_{\mathrm{O_2,ref}}$ a reference $O_2$ concentration at which the exchange current density is specified, $E^0$ the standard potential for the $O_2$ electrode, $F$ the Faraday's constant, $k^0$ the standard heterogeneous rate constant, $i_0$ the exchange current density ($i_0 = (n/s_{\mathrm{O_2}})Fk^0 C_{\mathrm{O_2,ref}}$), $n$ the number of electrons involved in $O_2$ reduction, $s_{\mathrm{O_2}}$ the stoichiometric coefficient for $O_2$, $R$ the universal gas constant, $T$ the temperature, $Z$ the position in the catalyst layer, $\alpha$ the cathodic transfer coefficient for $O_2$ reduction, while $\Phi_{\mathrm{s}}$ and $\Phi$ the potentials in the solid electronic conductor and polymer electrolyte phases, respectively.

Schlögl's equation for water transport in the membrane considers water movement due to both hydraulic pressure gradient $\mathrm{d}p/\mathrm{d}Z$, and electroosmotic drag, which is proportional to the potential gradient across the membrane $\mathrm{d}\Phi/\mathrm{d}Z$ [4]:

$$v_{\mathrm{m}} = -\frac{k_{\mathrm{p}}}{\mu}\frac{\mathrm{d}p}{\mathrm{d}Z} + \frac{k_\Phi}{\mu} z_{\mathrm{f}} C_{\mathrm{f}} \frac{\mathrm{d}\Phi}{\mathrm{d}Z} \quad (4)$$

with $C_{\mathrm{f}}$ fixed surface charge-site (i.e. sulfonate group) concentration; $k_{\mathrm{p}}$, $k_\Phi$ the hydraulic and electrokinetic membrane permeability, respectively; $z_{\mathrm{f}}$ the charge number; $v_{\mathrm{m}}$ the net water velocity in the membrane and $\mu$ the water (i.e. pore-fluid) dynamic viscosity.

The complete set of model equations for membrane, catalyst layer and gas diffuser are presented in the work of Bernardi and Verbrugge [4,5]. The associated list of variables, parameters and constants as applied in the dimensional analysis, are presented in Tables 1–3.

## 3. Dimensional analysis technique

In the present work the Quraishi–Fahidy method [23] has been applied to identify the dimensionless numbers describing the behaviour of the proton exchange membrane, catalyst layer and gas-diffusion layer according to the model outlined in the previous section. The Quraishi–Fahidy dimensional analysis technique comprises the following steps: (1) a list containing all the variables, parameters and constants with their respective SI units (using unity for dimensionless quantities) is complied, based on the governing model equations (algebraic, differential and/or integral); (2) each dimensional quantity on the list is divided by its SI units, generating quantity per unit ratios (or groups); (3) considering $N_{\mathrm{SI}}$ the total number of independent SI units involved in the model, a number of $N_{\mathrm{SI}}$ quantity-unit groups are selected such that to have the simplest possible mathematical form and all SI units encountered to be represented in the $N_{\mathrm{SI}}$ groups; (4) each of the $N_{\mathrm{SI}}$ number of groups is assigned a value of 1, designated as 'primary' groups; (5) the rest of the quantity-unit groups on the list are converted into an initial set of dimensionless numbers $\pi_i$, by substituting the units using the $N_{\mathrm{SI}}$ primary groups; (6) the initial set of dimensionless numbers $\pi_i$ is further transformed by algebraic manipulation in order to obtain as many as possible conventionally known dimensionless numbers and/or to generate new dimensionless numbers with clear physico-chemical meaning.

Tables 1–3 illustrate the outlined procedure and summarize the set of dimensionless numbers that are characteris-

Table 1
Dimensional analysis of the membrane

| Number | Quantity | Primary SI units | Quantity/units | Dimensionless numbers $\pi_i$ | | |
|---|---|---|---|---|---|---|
| | | | | Initial $\pi_i$ | Transform | Final $\pi_i$ |
| 1 | $i\ (=i_t)$ | $\mathrm{A\,m^{-2}}$ | $\frac{i\,\mathrm{m^2}}{\mathrm{A}}$ | 1 | – | – |
| 2 | $Z_m$ | m | $\frac{Z_m}{\mathrm{m}}$ | 1 | – | – |
| 3 | $\lvert z_f\rvert C_f$ | $\mathrm{mol\,m^{-3}}$ | $\frac{\lvert z_f\rvert C_f\,\mathrm{m^3}}{\mathrm{mol}}$ | 1 | – | – |
| 4 | $\rho$ | $\mathrm{kg\,m^{-3}}$ | $\frac{\rho\,\mathrm{m^3}}{\mathrm{kg}}$ | 1 | – | – |
| 5 | $\mu$ | $\mathrm{kg\,m^{-1}\,s^{-1}}$ | $\frac{\mu\,\mathrm{m\,s}}{\mathrm{kg}}$ | 1 | – | – |
| 6 | $D_{H^+}$ | $\mathrm{m^2\,s^{-1}}$ | $\frac{D_{H^+}\,\mathrm{s}}{\mathrm{m^2}}$ | $\frac{D_{H^+}\rho}{\mu}$ | $\frac{1}{\pi_1}$ | $\pi_1 = \frac{\mu}{D_{H^+}\rho}$ |
| 7 | $\left(\frac{n}{s_{H^+}}\right)F$ | $\mathrm{A\,s\,mol^{-1}}$ | $\frac{nF\,\mathrm{mol}}{s_{H^+}\,\mathrm{A\,s}}$ | $\frac{nF\lvert z_f\rvert C_f\mu}{iZ_m s_{H^+}\rho}$ | $\frac{1}{\pi_2}$ | $\pi_2 = \frac{iZ_m s_{H^+}\rho}{nF\lvert z_f\rvert C_f\mu}$ |
| 8 | $C_{O_2}$ | $\mathrm{mol\,m^{-3}}$ | $\frac{C_{O_2}\,\mathrm{m^3}}{\mathrm{mol}}$ | $\frac{C_{O_2}}{\lvert z_f\rvert C_f}$ | – | $\pi_3 = \frac{C_{O_2}}{\lvert z_f\rvert C_f}$ |
| 9 | $k_p\Delta p$ | $\mathrm{kg\,m\,s^{-2}}$ | $\frac{(k_p\Delta p)\,\mathrm{s^2}}{\mathrm{kg\,m}}$ | $\frac{(k_p\Delta p)\rho}{\mu^2}$ | – | $\pi_4 = \frac{(k_p\Delta p)\rho}{\mu^2}$ |
| 10 | $k_\Phi\Delta\Phi$ | $\mathrm{kg\,m^4\,A^{-1}\,s^{-3}}$ | $\frac{(k_\Phi\Delta\Phi)\,\mathrm{A\,s^3}}{\mathrm{kg\,m^4}}$ | $\frac{(k_\Phi\Delta\Phi)i\rho^2 Z_m}{\mu^3}$ | $\pi_5\pi_2\pi_4$ | $\pi_5 = \frac{n\lvert z_f\rvert C_f F(k_\Phi\Delta\Phi)}{s_{H^+}k_p\Delta p}$ |
| 11 | $\kappa$ | $\mathrm{A^2\,s^3\,kg^{-1}\,m^{-3}}$ | $\frac{\kappa\,\mathrm{kg\,m^3}}{\mathrm{A^2\,s^3}}$ | $\frac{\kappa\mu^3}{i^2Z_m^4\rho^2}$ | $\frac{\pi_6}{\pi_2^2}$ | $\pi_6 = \frac{\kappa\mu s_{H^+}^2}{(nF\lvert z_f\rvert C_f)^2 Z_m^2}$ |
| 12 | $D_{O_2}$ | $\mathrm{m^2\,s^{-1}}$ | $\frac{D_{O_2}\,\mathrm{s}}{\mathrm{m^2}}$ | $\frac{D_{O_2}\rho}{\mu}$ | $\frac{1}{\pi_7}$ | $\pi_7 = \frac{\mu}{D_{O_2}\rho}$ |

tic for the membrane, catalyst and gas-diffusion layer, respectively. For all three cases $N_{SI} = 5$ (i.e., kg, m, s, mol and A).Thus, the proton exchange membrane could be characterized by 7 dimensionless numbers, $\pi_1, \ldots, \pi_7$, the catalyst layer by 11 numbers, $\pi_0$, $\pi_8, \ldots, \pi_{17}$, while the gas-diffusion (or backing) layer could be described using 8 numbers, $\pi_{18}, \ldots, \pi_{25}$. The physico-chemical significance and implications of the obtained dimensionless numbers for the

Table 2
Dimensional analysis of the cathode catalyst layer

| Number | Quantity | Primary SI units | Quantity/units | Dimensionless numbers $\pi_i$ | | |
|---|---|---|---|---|---|---|
| | | | | Initial $\pi_i$ | Transform | Final $\pi_i$ |
| 1 | $i$ | $\mathrm{A\,m^{-2}}$ | $\frac{i\,\mathrm{m^2}}{\mathrm{A}}$ | 1 | – | – |
| 2 | $Z_c$ | m | $\frac{Z_c}{\mathrm{m}}$ | 1 | – | – |
| 3 | $C_{O_2}$ | $\mathrm{mol\,m^{-3}}$ | $\frac{C_{O_2}\,\mathrm{m^3}}{\mathrm{mol}}$ | 1 | – | – |
| 4 | $\rho$ | $\mathrm{kg\,m^{-3}}$ | $\frac{\rho\,\mathrm{m^3}}{\mathrm{kg}}$ | 1 | – | – |
| 5 | $\mu$ | $\mathrm{kg\,m^{-1}\,s^{-1}}$ | $\frac{\mu\,\mathrm{m\,s}}{\mathrm{kg}}$ | 1 | – | – |
| 6 | $e^{-f(\Phi_s-\Phi-E^0)}$ | – | – | $e^{-f(\Phi_s-\Phi-E^0)}$ | – | $\pi_0 = e^{-f(\Phi_s-\Phi-E^0)}$ |
| 7 | $D_{O_2,c}$ | $\mathrm{m^2\,s^{-1}}$ | $\frac{D_{O_2,c}\,\mathrm{s}}{\mathrm{m^2}}$ | $\frac{D_{O_2,c}\rho}{\mu}$ | $\frac{1}{\pi_8}$ | $\pi_8 = \frac{\mu}{D_{O_2,c}\rho}$ |
| 8 | $a_c k^0$ | $\mathrm{s^{-1}}$ | $(a_c k^0)\,\mathrm{s}$ | $\frac{(a_c k^0)\rho Z_c^2}{\mu}$ | $\frac{\pi_9}{\pi_8}$ | $\pi_9 = \frac{(a_c k^0)Z_c^2}{D_{O_2,c}}$ |
| 9 | $\left(\frac{n}{s_{O_2}}\right)F$ | $\mathrm{A\,s\,mol^{-1}}$ | $\frac{nF\,\mathrm{mol}}{s_{O_2}\,\mathrm{A\,s}}$ | $\frac{nFC_{O_2}\mu}{s_{O_2}iZ_c\rho}$ | $\frac{\pi_8}{\pi_{10}}$ | $\pi_{10} = \frac{iZ_c s_{O_2}}{nFD_{O_2,c}C_{O_2}}$ |
| 10 | $i_t$ | $\mathrm{A\,m^{-2}}$ | $\frac{i_t\,\mathrm{m^2}}{\mathrm{A}}$ | $\frac{i_t}{i}$ | – | $\pi_{11} = \frac{i_t}{i}$ |
| 11 | $\lvert z_f\rvert C_f$ | $\mathrm{mol\,m^{-3}}$ | $\frac{\lvert z_f\rvert C_f\,\mathrm{m^3}}{\mathrm{mol}}$ | $\frac{\lvert z_f\rvert C_f}{C_{O_2}}$ | – | $\pi_{12} = \frac{\lvert z_f\rvert C_f}{C_{O_2}}$ |
| 12 | $k_{p,c}\Delta p$ | $\mathrm{kg\,m\,s^{-2}}$ | $\frac{(k_{p,c}\Delta p_c)\,\mathrm{s^2}}{\mathrm{kg\,m}}$ | $\frac{(k_{p,c}\Delta p_c)\rho}{\mu^2}$ | – | $\pi_{13} = \frac{(k_{p,c}\Delta p_c)\rho}{\mu^2}$ |
| 13 | $k_{\Phi,c}\Delta\Phi$ | $\mathrm{kg\,m^4\,A^{-1}s^{-3}}$ | $\frac{(k_{\Phi,c}\Delta\Phi)\,\mathrm{A\,s^3}}{\mathrm{kg\,m^4}}$ | $\frac{(k_{\Phi,c}\Delta\Phi)i\rho^2 Z_c}{\mu^3}$ | $\frac{\pi_{14}\pi_{13}\pi_{10}}{\pi_8\pi_{12}}$ | $\pi_{14} = \frac{n\lvert z_f\rvert C_f F(k_{\Phi,c}\Delta\Phi)}{s_{O_2}k_{p,c}\Delta p}$ |
| 14 | $\Delta\Phi_s$ | $\mathrm{kg\,m^2\,A^{-1}\,s^{-3}}$ | $\frac{\Delta\Phi_s\,\mathrm{A\,s^3}}{\mathrm{kg\,m^2}}$ | $\frac{\Delta\Phi_s i Z_c^3\rho^2}{\mu^3}$ | $\frac{\pi_{15}\pi_{13}\pi_{10}}{\pi_8\pi_{12}}$ | $\pi_{15} = \frac{n\lvert z_f\rvert C_f F\Delta\Phi_s Z_c^2}{s_{O_2}k_{p,c}\Delta p}$ |
| 15 | $\kappa_c$ | $\mathrm{A^2\,s^3\,kg^{-1}\,m^{-3}}$ | $\frac{\kappa_c\,\mathrm{kg\,m^3}}{\mathrm{A^2\,s^3}}$ | $\frac{\kappa_c\mu^3}{i^2Z_c^4\rho^2}$ | $\pi_{16}\left(\frac{\pi_8\pi_{12}}{\pi_{10}}\right)^2$ | $\pi_{16} = \frac{\kappa_c\mu s_{O_2}^2}{(n\lvert z_f\rvert FC_f)^2 Z_c^2}$ |
| 16 | $\sigma_c$ | $\mathrm{A^2\,s^3\,kg^{-1}\,m^{-3}}$ | $\frac{\sigma_c\,\mathrm{kg\,m^3}}{\mathrm{A^2\,s^3}}$ | $\frac{\sigma_c\mu^3}{i^2Z_c^4\rho^2}$ | $\pi_{17}\left(\frac{\pi_8\pi_{12}}{\pi_{10}}\right)^2$ | $\pi_{17} = \frac{\sigma_c\mu s_{O_2}^2}{(n\lvert z_f\rvert FC_f)^2 Z_c^2}$ |

Table 3
Dimensional analysis of the gas diffusion-backing layer

| Number | Quantity | Primary SI units | Quantity/units | Dimensionless numbers $\pi_i$ | | |
|---|---|---|---|---|---|---|
| | | | | Initial $\pi_i$ | Transform | Final $\pi_i$ |
| 1 | $i_s$ ($=i_t$) | $\mathrm{A\,m^{-2}}$ | $\frac{i_s\,\mathrm{m^2}}{\mathrm{A}}$ | 1 | – | – |
| 2 | $Z_d$ | m | $\frac{Z_d}{\mathrm{m}}$ | 1 | – | – |
| 3 | $\rho$ | $\mathrm{kg\,m^{-3}}$ | $\frac{\rho\,\mathrm{m^3}}{\mathrm{kg}}$ | 1 | – | – |
| 4 | $\mu$ | $\mathrm{kg\,m^{-1}\,s^{-1}}$ | $\frac{\mu\,\mathrm{m\,s}}{\mathrm{kg}}$ | 1 | – | – |
| 5 | $\Delta x_{O_2}\frac{p_d}{RT}$ | $\mathrm{mol\,m^{-3}}$ | $\frac{\Delta x_{O_2}\,p_d\,\mathrm{m^3}}{RT\,\mathrm{mol}}$ | 1 | – | – |
| 6 | $D_{N_2-O_2,d}$ | $\mathrm{m^2\,s^{-1}}$ | $\frac{D_{N_2-O_2,d}\,\mathrm{s}}{\mathrm{m^2}}$ | $\frac{D_{N_2-O_2,d}\rho}{\mu}$ | $\frac{1}{\pi_{18}}$ | $\pi_{18}=\frac{\mu}{D_{N_2-O_2,d}\rho}$ |
| 7 | $D_{w-air,d}$ | $\mathrm{m^2\,s^{-1}}$ | $\frac{D_{w-air,d}\,\mathrm{s}}{\mathrm{m^2}}$ | $\frac{D_{w-air,d}\rho}{\mu}$ | $\frac{1}{\pi_{19}}$ | $\pi_{19}=\frac{\mu}{D_{w-air,d}\rho}$ |
| 8 | $x_{w,sat}$ $\left(=\frac{p_{w,sat}}{p_d}\right)$ | – | – | $x_{w,sat}$ | – | $\pi_{20}=x_{w,sat}$ |
| 9 | $x_{N_2}$ | – | – | $x_{N_2}$ | – | $\pi_{21}=x_{N_2}$ |
| 10 | $v_{0,d}$ | $\mathrm{m\,s^{-1}}$ | $\frac{v_{0,d}\,\mathrm{s}}{\mathrm{m}}$ | $\frac{v_{0,d}\rho Z_d}{\mu}$ | – | $\pi_{22}=\frac{v_{0,d}\rho Z_d}{\mu}$ |
| 11 | $\left(\frac{n}{s_{O_2}}\right)F$ | $\mathrm{A\,s\,mol^{-1}}$ | $\frac{nF\,\mathrm{mol}}{s_{O_2}\,\mathrm{A\,s}}$ | $\frac{nF\Delta x_{O_2}p_d\mu}{i_s Z_d s_{O_2}\rho RT}$ | $\frac{\pi_{18}}{\pi_{23}}$ or $\frac{\pi_{19}}{\pi_{23,w}}$ | $\pi_{23}=\frac{i_s s_{O_2} Z_d RT}{nFD_{N_2-O_2,d}\Delta x_{O_2}p_d}$ or $\pi_{23,w}=\frac{i_s s_{O_2} Z_d RT}{nFD_{w-air_2,d}\Delta x_{O_2}p_d}$ |
| 12 | $\Delta\Phi_s$ | $\mathrm{kg\,m^2\,A^{-1}\,s^{-3}}$ | $\frac{\Delta\Phi_s\,\mathrm{A\,s^3}}{\mathrm{kg\,m^2}}$ | $\frac{\Delta\Phi_s i_s Z_d^3\rho^2}{\mu^3}$ | $\frac{\pi_{24}\pi_{22}\pi_{23}}{\pi_{18}}$ | $\pi_{24}=\frac{nF\Delta\Phi_s Z_d}{s_{O_2}v_{0,d}\mu}\left(\Delta x_{O_2}\frac{p_d}{RT}\right)$ |
| 13 | $\sigma_d$ | $\mathrm{A^2\,s^3\,kg^{-1}\,m^{-3}}$ | $\frac{\sigma_d\,\mathrm{kg\,m^3}}{\mathrm{A^2\,s^3}}$ | $\frac{\sigma_d\mu^3}{i^2Z_d^4\rho^2}$ | $\pi_{25}\frac{\pi_{18}^2}{\pi_{23}^2}$ | $\pi_{25}=\frac{\sigma_d\mu}{\left(\frac{n}{s_{O_2}}F\Delta x_{O_2}\frac{p_d}{RT}\right)^2 Z_d^2}$ |

membrane-gas diffusion electrode assembly analysis are discussed in the next paragraph.

Furthermore, the relation among dimensionless numbers (i.e. correlating equations) can be represented as

$$\pi_n = \Psi\{\pi_j\,|\,j=1,\ldots,(N_d-1)\},\quad n\neq j, \tag{5}$$

where $N_d$ is the number of dimensionless groups describing the system, $\pi_n$ a dimensionless number containing the dependent variable, and $\Psi$ a correlating function, that is either monomial or non-monomial [20]. The monomial (i.e. power series) form is

$$\pi_n = y_0\pi_1^{y_1}\pi_2^{y_2}\cdots\pi_{N_d-1}{}^{y_{N_d-1}} \tag{6}$$

with $y_j\,|\,j=1,\ldots,(N_d-1)$ numeric exponents and $y_0$ a constant coefficient. The numeric exponents and constant could be determined by regression using experimental data relating the dependent variable entering the expression of $\pi_n$ to independent variables and parameters composing $\pi_j$, coupled with asymptotic and speculative analysis as shown by Churchill and co-workers [25–27].

The case when $\Psi$ is of non-monomial form (i.e., it includes one or more of the following: addition, subtraction, or transcendental functions of $\pi_j$) leads to multiple coefficients $y_0$ (at least two [20]). Therefore, the quantitative interpretation and analysis of the dimensionless correlation becomes more difficult as compared to the monomial function situation. To detect a non-monomial $\Psi$, the typical procedure is to assume initially a monomial form and to prove it leads to a contradiction or impossibility [20].

In the next paragraph the characteristic dimensionless numbers and the applicability of monomial correlating equations for the membrane, catalyst layer and gas-diffusion layer, are discussed.

## 4. Results and discussion

### *4.1. Dimensionless numbers and monomial correlating equations for the membrane*

Table 1 shows the seven dimensionless numbers, which are characteristic for the membrane, obtained by applying the Quraishi–Fahidy technique to the variables and parameters encountered in the model. The dimensionless ratios $\pi_1$ and $\pi_7$ are membrane Schmidt numbers relating the pore-fluid (i.e. water) viscosity to the proton and dissolved $O_2$ diffusion coefficients, respectively, whilst $\pi_3$ is simply the concentration ratio of dissolved $O_2$ and fixed charges.

The dimensionless number $\pi_2$ (Table 1 and Eq. (7)) on the other hand is new, and it relates the current density $i$, membrane thickness $Z_m$, and the fixed surface charge concentration $|z_f|C_f$ (which, based on electroneutrality is equal to the membrane proton concentration, $|z_f|C_f = C_{H^+}$), with the pore-fluid dynamic viscosity $\mu$ and density $\rho$. Moreover, $\pi_2$ could be expressed as

$$\pi_2 = \frac{iZ_m s_{H^+}\rho}{nF|z_f|C_f\mu} = \frac{iZ_m s_{H^+}}{nFD_{H^+}C_{H^+}}\frac{D_{H^+}\rho}{\mu} = \frac{\pi_2^*}{\pi_1}. \tag{7}$$

In Eq. (7), the ratio $\pi_2^*$ has an expression mathematically similar but conceptually different than the mass transfer Nusselt number for electrochemical systems $Nu_E$, introduced by Ibl [28]:

$$Nu_E = \frac{il}{nFD\Delta C}, \tag{8}$$

where $\Delta C$ is the concentration difference between the bulk and electrode interface, $D$ the diffusion coefficient, $l$ the characteristic length and $n$ the number of electrons. For mass transfer limiting conditions, i.e. $\Delta C = C_b$ and $i = i_L$, the dimensionless ratio given by Eq. (8) is commonly referred to as the Sherwood number [23,29].

Considering that the proton concentration in the membrane is constant, the interpretation given for $Nu_E$ is not applicable to $\pi_2^*$. Substituting the Nernst–Einstein equation, $D_{H^+} = \frac{u_{H^+}RT}{F}$, which is based on the commonly employed infinite-dilution assumption, shows that $\pi_2^*$ expresses the ratio between the total (i.e. migration plus convection) proton flux in the membrane pore fluid $\left(= \frac{is_{H^+}}{nF}\right)$ and the migration flux corresponding to a unitary, 1 V, potential difference across the membrane $\left(= \frac{u_{H^+}C_{H^+}}{Z_m}\right)$.

It must be noted that $D_{H^+}$ increases with membrane water content [30], which in turn is a function of the operating conditions of the fuel cell. Furthermore, the water content across the membrane thickness might not be uniform [31] (e.g., the cathode side could be more hydrated than the anode side) hence, $D_{H^+}$ and implicitly $\pi_2^*$ could have different values across the thickness of the membrane. The dimensionless number $\pi_2$ on the other hand (Eq. (7)), is constant under given operating conditions.

The dimensionless number $\pi_4$ in Table 1 is a ratio of inertial to viscous forces with respect to the membrane pore-fluid, where the inertial force is related to the hydraulic permeability–pressure difference product $k_p\Delta p$ (Darcy's law). Thus, $\pi_4$ is a membrane pore-fluid Reynolds number, $Re_m$.

Additionally, two new dimensionless numbers have been identified, which were not discussed previously in the literature, $\pi_5$ and $\pi_6$, respectively (Table 1). The expression of $\pi_5$ includes the potential difference (or drop) across the membrane-electrolyte $\Delta\Phi$, in relation with certain physicochemical properties of the membrane such as electrokinetic and hydraulic permeabilities, $k_\Phi$ and $k_p$, and fixed-surface charge concentration $|z_f|C_f$. Since $n = 4$ and $s_{H^+} = 4$ (Eq. (2)), $\pi_5$ is given by

$$\pi_5 = \frac{|z_f|FC_f(k_\Phi\Delta\Phi)}{k_p\Delta p} \equiv \frac{\text{electrical force}}{\text{inertial force}}. \tag{9}$$

Thus, $\pi_5$ could be interpreted as the ratio between the pore water velocity induced by the electrical force (electroosmotic drag) and the velocity due purely to the inertial force (see also Eq. (4)). $\Delta p$ is defined here as the hydraulic pressure difference between the cathode and anode side of the membrane.

The dimensionless ratio $\pi_6$ on the other hand, relates the bulk (or actual) specific ionic conductivity of the membrane $\kappa$ to the surface-convective conductivity, which is related to the fixed surface charge density $q_f$ (C m$^{-2}$):

$$\pi_6 = \frac{\kappa\mu}{(|z_f|FC_f)^2Z_m^2} = \frac{\kappa\mu}{q_f^2} \equiv \frac{\text{bulk (actual) proton conductivity}}{\text{surface-convective proton conductivity}}. \tag{10}$$

In the analysis of electrokinetic phenomena, Newman introduced a dimensionless ratio conceptually similar to $\frac{1}{\pi_6}$, i.e., $\frac{q_{dl}^2}{\mu\kappa}$, where $q_{dl}$ is the surface charge density in the diffuse double layer and $\kappa$ is the specific conductivity at the center of the capillary. The surface-convective conductivity is proportional to $\frac{q_{dl}^2}{\mu}$ and it is due to the convective transport of ions by the fluid moving in the diffuse layer under the action of the electric field [32]. This concept is applicable to the proton exchange membrane, where the convective surface proton conductivity can be considered proportional to the square of the fixed surface charge density $q_f$.

Thus, $\pi_6$ compares the proton conductivity of the membrane $\kappa$, which is dependent on the actual operating conditions (e.g., membrane water content and temperature as shown by Eq. (11)), with the intrinsic surface-convective conductivity of the membrane determined by the physicochemical properties of the membrane.

Based on the studies of Zawodinski et al. [33], Meier and Eigenberger [31] established the following equation describing the water content $\lambda$ and temperature $T$ dependence of $\kappa$ (S m$^{-1}$):

$$\kappa = (0.46\lambda - 0.25)\exp\left[-1190\left(\frac{1}{T} - \frac{1}{298.15}\right)\right], \quad 0 < \lambda < 30. \tag{11}$$

However, in operating fuel cells it is difficult to determine experimentally either the in situ water content or the specific conductivity of the membrane. Furthermore, the membrane specific conductivity could be anisotropic across its thickness [31,34]. Therefore, in the absence of relevant data under fuel cell operating conditions, in the expression of $\pi_6$, $\kappa$ could be approximated with the in situ specific conductivity at zero current (i.e., at open-circuit conditions) $\kappa_0$.

Büchi and Scherer reported for Nafion® membranes of 1100 g eq$^{-1}$ equivalent weight, that the in situ specific conductivity at zero current $\kappa_0$, was approximately constant at given temperature and humidification conditions for membrane thickness greater than about 150 μm (e.g., 10 S m$^{-1}$ at 333 K, dry $O_2$ feed/humid $H_2$, for N105 and N117 membranes of 'wet' thickness 163 and 203 μm, respectively) [34]. However, the same authors observed that for thinner membranes (i.e., 'wet' thickness less than about 150 μm such as N112: 60 μm, NE 1135: 88 μm and N115: 148 μm) the thin-

ner the membrane the lower the specific conductivity at zero current [34]. Discounting potential experimental errors, these differences were explained by conductivity anisotropicity at the membrane boundary layer adjacent to the gas-diffusion electrode structure [34].

The seven dimensionless numbers given in Table 1 in conjunction with a correlating function $\Psi$ could be employed to describe and analyze the membrane behaviour. To simplify the correlating function, the effect of the dissolved $O_2$ concentration on the membrane potential drop, expressed by $\pi_3$ and $\pi_7$, was neglected. This assumption implies a complete consumption of $O_2$ in the catalyst layer.

Employing a monomial correlating function (Eq. (6)), and considering $\Delta\Phi$ the dependent variable, the membrane behaviour could be described as

$$\pi_5 = y_{0,m}\pi_2^{y_2}\pi_4^{y_4}\pi_4^{y_6}, \tag{12}$$

$$\left(\frac{|z_f|FC_f(k_\Phi\Delta\Phi)}{k_p\Delta p}\right) = y_{0,m}\left(\frac{iZ_m s_{H^+}\rho}{nF\,|z_f|\,C_f\mu}\right)^{y_2} \times \left(\frac{(k_p\Delta p)\rho}{\mu^2}\right)^{y_4}\left(\frac{\kappa_0\mu}{q_f^2}\right)^{y_6}. \tag{13}$$

The correlating equation (13) describes in a dimensionless form, the potential drop across the membrane as a function of the open-circuit specific conductivity, membrane physico-chemical properties and fuel cell operating conditions. Next examples are given for the determination of $y_2$, $y_4$, $y_6$ and $y_{0,m}$ using literature studies of the membrane ohmic potential drop.

Srinivasan et al. presented experimentally measured cell voltage data obtained at 368 K with $H_2/O_2$ at 4/5 atm, as a function of membrane physico-chemical characteristics (i.e., Nafion® and proprietary Dow) and thickness (i.e., 1100 g eq$^{-1}$ Nafion® of 50, 100 and 175 μm 'dry' thickness). The membrane ohmic drop was estimated from the cell voltage using a proposed cell polarization equation and afferent kinetic parameters [35]. Furthermore, Meier and Eigenberger reported the membrane ohmic drop as a function of current density for Nafion® membranes N112, NE1135, N115 and N117, at 353 K with $H_2/O_2$ at 2/2 bar [31].

Figs. 2 and 3 show the dependence of $\pi_5$ on $\pi_2$, extracted from the data reported in references [35] and [31], respectively, and fitted to Eq. (12) extrapolated to $\pi_2 = 0$. The hydraulic pressure drop was 1 atm in Fig. 2 and 0.1 atm was assumed for the conditions relevant to Fig. 3. The current density ranges were: 5000–14,000 A m$^{-2}$ (Fig. 2) and 2000–12,500 A m$^{-2}$ (Fig. 3), respectively. The membrane physico-chemical properties are summarized in Table A1 (Appendix A). The literature data was fitted to Eq. (12) written as $\pi_5 = y^*_{0,m}\pi_2^{y_2}$.

Figs. 2 and 3 show that the 'thin' Nafion membranes ('dry' thickness ≤ 100 μm such as N112) and the Dow membrane, were characterized by a linear dependence of $\pi_5$ on $\pi_2$. However, for Nafion 'dry' thickness of 127 μm (N115, Fig. 3) and

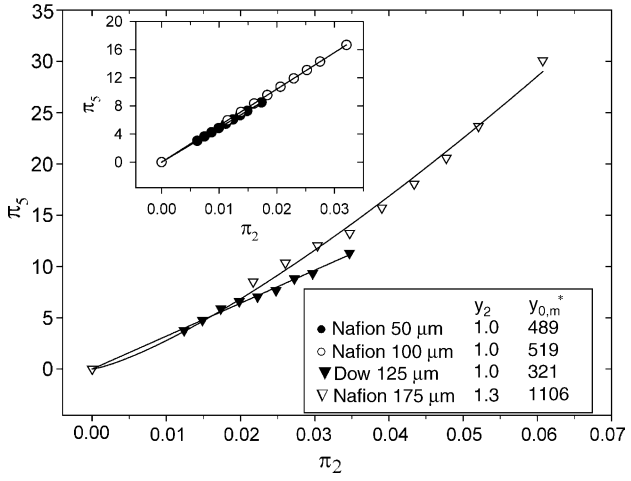


Fig. 2. Correlations between dimensionless numbers $\pi_5$ and $\pi_2$ for selected Nafion and Dow membranes. Data points from the study of Srinivasan et al. [35]. Dry membrane thickness: (●) 50 μm (Nafion), (○) 100 μm (Nafion), (▼) 125 μm (Dow), (▽) 175 μm (Nafion). $\Delta p$ = 1 atm, 368 K.

175–183 μm (N117, Figs. 2 and 3) a deviation from linearity was obtained, reflected by $y_2$ of 1.3. In the case of uniformly and well-hydrated membranes a linear behaviour is expected for the membrane potential drop as a function of current density described by Ohm's law [39]. The latter condition and, therefore, the applicability of Ohm's law is likely to be met at low current densities and in the case of 'thin' membranes (e.g., up to about 100 μm 'dry' thickness). These criteria can be better expressed using the dimensionless number $\pi_2$ (Eq. (7)) by defining a linear-region limiting $\pi_{2,l}$ ratio. Based on Fig. 2, $\pi_{2,l} \cong 0.035$, whilst $\pi_{2,l} \cong 0.02$ in the case of Fig. 3. Therefore, when $\pi_2 \leq \pi_{2,l}$ the membrane ohmic drop can be estimated with $\Delta\Phi = iZ_m/\kappa_0$.

However, for $\pi_2 > \pi_{2,l}$ (i.e. a combination of high current density, 'thick' membrane and/or low fixed charge-site concentration, Eq. (7)) the ohmic drop behaviour as a func-

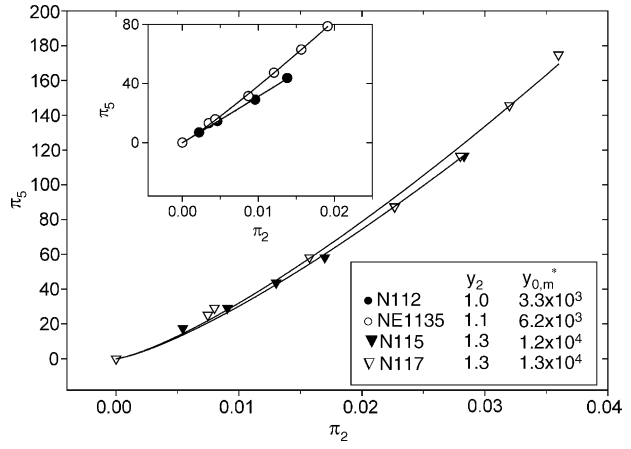


Fig. 3. Correlations between dimensionless numbers $\pi_5$ and $\pi_2$ for selected Nafion membranes. Data points from the study of Meier and Eigenberger [31]. Nafion membrane types: (●) N112, (○) NE1135, (▼) N115, (▽) N117. $\Delta p$ = 0.1 atm, 353 K.

Table A1
Membrane properties

| Membrane type | Typical 'dry' thickness (μm) | Basis weight[a] ($kg\,m^{-2}$) | 'Wet' thickness[c] (μm) | Acid capacity ($eq\,kg^{-1}$) | Fixed charge-site concentration $C_f$, on 'wet' membrane basis ($mol\,m^{-3}$)[f] |
|---|---|---|---|---|---|
| N112 | 51[a] | 0.10 | 58 | 0.89[d] | 1534 |
| NE1135 | 89[a] | 0.19 | 102 | idem | 1658 |
| N115 | 127[a] | 0.25 | 145 | idem | 1534 |
| N117 | 183[a] | 0.36 | 209 | idem | 1533 |
| Dow | 125–130[b] | NA | 148 | 1.13[b] | 1918[e] |

[a] Membrane conditioned at 296 K and 50% relative humidity (RH) [36]. Note the Nafion membranes of 50, 100 and 175 μm dry thickness from Ref. [35] were considered to have similar characteristics as N112, NE1135 and N117, respectively.
[b] Refs. [35,37].
[c] Estimated from the 'dry' thickness using a 14% thickness increase from 296 K at 50% RH to water soaked at 373 K [36].
[d] From Ref. [36].
[e] Estimated assuming a 25% higher fixed charge-site concentration for the Dow membrane as compared to N117 [5].
[f] The $C_f$ values for the Nafion membranes are close to the average of $1591\,mol\,m^{-3}$ given in Ref. [38] for the 1100 series Nafion.

tion of current density deviates from linearity. This is further supported by a separate study showing the increase of the experimentally measured in situ membrane resistance with current density for membrane 'wet' thickness greater than about 150 μm (such as N117, Appendix A and Table A1) [34]. Thus, a value of $y_2 > 1$ in Eq. (13) shows that the membrane resistance increases with current density, possibly due to dehydration of some parts of the membrane (most likely on the anode side) during the operation of the fuel cell.

Furthermore, Eq. (13) estimates fairly well the membrane thickness effect on the ohmic potential drop. In the experimental study of Büchi and Scherer, at a current density of $5000\,A\,m^{-2}$ for N117 approximately a 2.5 times increase of the in situ membrane resistance was projected when the 'wet' thickness of N117 was doubled from 200 to 400 μm [34]. According to Eq. (13) for N117 with $y_2 = 1.3$, doubling the thickness at a constant current density implies an ohmic drop increase by a factor of about 2.5.

It is interesting to note at this point, that in the phenomenological modeling of the Ballard Mark IV fuel cell Amphlett et al. established a linear dependence for the internal cell resistance (due mainly to membrane N117 ohmic loss) as a function of current density [19]. However, the same authors also noted that quadratic and other forms of non-linear effects for current density and temperature could be also possible. Thus, the non-linear dependence of membrane ohmic loss as a function of current is plausible as suggested here for N117.

Regarding the exponent $y_4$ in Eq. (13), which reflects the water permeability effect on the membrane ohmic drop, unfortunately neither the study by Srinivasan et al. nor the one by Meier and Eigenberger do not present enough data that could be used to estimate $y_4$ independently. However, based on the work of Springer et al. showing that the high-frequency cell resistance under well-humidified conditions is independent of the pressure difference $\Delta p$ [40], it is considered that under well-humidified conditions $\Delta\Phi$ is virtually unaffected by $k_p\Delta p$ (i.e. the streaming potential contribution can be neglected). The well-humidified membrane condition yields $y_4$ equal to $-1$. Dehydration on the other hand, is characterized by $y_4 < -1$, since an increase of $k_p\Delta p$ would decrease the ohmic potential drop. In the present work for N117 it was assumed that $y_4 = -1.05$, allowing for approximately a 10% decrease of $\Delta\Phi$ for a 10-fold increase of $k_p\Delta p$.

The exponent $y_6$ can be estimated from a fit of $\pi_5$ as a function of $\pi_6$ corresponding to different open-circuit conditions of humidity and/or temperature, effecting $\kappa_0$ (Eqs. (10) and (11)). In the expression of $\pi_6$, Eq. (10), the fixed surface charge density $q_f$, is defined per geometric cross-sectional area. However, it is more relevant to express $q_f$ as the charge per total (or effective) membrane surface area. The latter was calculated using the equation presented by van der Stegen et al. assuming a straight and parallel cylindrical pore model for the membrane [41]:

$$q_f = \frac{(1-\theta_m)|z_f|C_f F r_p}{2\theta_m}, \tag{14}$$

where $r_p$ is the membrane pore radii (m) and $\theta_m$ the water uptake of the membrane per volume basis ($m^3\,m^{-3}$). An average pore radius of 2 nm was assumed for the Nafion membranes, based on the study by Divisek et al. indicating that the latter average pore radius corresponds to the highest fraction of water uptake and pore volume [42]. The pore size of the Dow membrane on the other hand, is about 25% smaller compared to Nafion of similar thickness [43], therefore, $r_p = 1.5$ nm.

For membranes with sulfonate charge sites, $\theta_m$ can be estimated by [41]:

$$\theta_m = 0.646 + 0.604\gamma_w + 0.112\gamma_w^2 - 0.935\mathrm{EW} + 0.36\mathrm{EW}^2 - 0.441\mathrm{EW}\gamma_w, \tag{15}$$

where EW is the membrane equivalent weight ($kg\,eq^{-1}$, $1.123\,kg\,eq^{-1}$ Nafion and $0.885\,kg\,eq^{-1}$ Dow, see Appendix A) and $\gamma_w$ is the water activity coefficient (~0.9 to 0.975, for $\lambda = 9$–14 [38]).

From Eqs. (14) and (15) for the conditions explored in Figs. 2 and 3 it was found that $\theta_m = 0.21\,m^3\,m^{-3}$ and $q_f = 0.55$–$0.6\,C\,m^{-2}$ for the Nafion membranes whilst, $\theta_m = 0.45\,m^3\,m^{-3}$ and $q_f = 0.17\,C\,m^{-2}$ for the Dow membrane, respectively.

As an example for the determination of $y_6$ the N117 membrane was employed. The $\pi_6$ ratio between the conditions of Figs. 3 and 2, was calculated using $\kappa_0 = 13.2\,\mathrm{S\,m^{-1}}$ (353 K and $\lambda = 16$) and $10.3\,\mathrm{S\,m^{-1}}$ (368 K and $\lambda = 11$), respectively. From Eq. (13), using the $\pi_5$ ratio between Figs. 3 and 2 (i.e., equal to 11.5 for $\pi_2 = \text{const.}$) and the previously determined exponents, yielded $y_6 = -1.3$ for N117.

Furthermore, it is interesting to note that the $\pi_6$ values were between 0.010 and 0.016 for the Nafion 1100 series and 0.23 for the Dow membrane, respectively. These ratios indicate that the actual membrane conductivity for Nafion is up to two orders of magnitude smaller than the surface-convective conductivity supporting, therefore, the hypothesis that the membrane proton conductivity is not predominantly surface mechanism-based [44]. However, the approximately twenty times higher $\pi_6$ ratio for the Dow membrane compared to the Nafion, suggests that in the case of the former the surface-convective mechanism plays a more significant role.

Based on the proposed dimensionless groups and monomial correlating function, for $\pi_2 > \pi_{2,l}$ the ohmic drop for the N117 membrane under the conditions presented in Figs. 2 and 3 can be expressed as

$$\left(\frac{|z_f|\,FC_f(k_\Phi \Delta\Phi)}{k_p \Delta p}\right) = 5\times 10^{-3}\left(\frac{iZ_m s_{H^+}\rho}{nF\,|z_f|\,C_f\mu}\right)^{1.3}\left(\frac{(k_p\Delta p)\rho}{\mu^2}\right)^{-1.05}\left(\frac{\kappa_0\mu}{q_f^2}\right)^{-1.3}. \tag{16}$$

Note that as discussed previously, in Eq. (16) the specific conductivity at open-circuit conditions is used, which is more readily accessible experimentally and/or by calculation as compared to the in situ specific conductivity.

The coefficient $y_{0,m}$ in Eq. (16), can be interpreted as the value of $\pi_5$ in the particular case when $\pi_2 = \pi_4 = \pi_6 = 1$. Since typical values of $\pi_4$ and $\pi_6$ are about $10^{-4}$ to $10^{-3}$ and $10^{-2}$ to $10^{-1}$, respectively, the special case of $\pi_4 = \pi_6 = 1$ indicates a combination of high hydraulic water permeability and ionic conductivity, therefore, it is expected that $y_{0,m} < 1$ (see also Eq. (9)).

### 4.2. Dimensionless numbers and monomial correlating equations for the catalyst layer

Table 2 shows the dimensionless numbers describing the catalyst layer. The exponential term containing the electrode potential ($\Phi_s - \Phi$) was assigned to the dimensionless number $\pi_0$. Equivalent forms for $\pi_0$ can be written in terms of overpotential $\eta = \Phi_s - \Phi - E^0$ (as defined in Ref. [39]) and Tafel slope for $O_2$ reduction $b = 2.3RT/\alpha F$:

$$\pi_0 = \exp(-f(\Phi_s - \Phi - E^0)) = \exp\left(-\frac{\alpha F}{RT}\eta\right) = \exp\left(-\frac{2.3}{b}\eta\right), \tag{17}$$

where commonly the transfer coefficient $\alpha = 0.6 - 1$ based on experimentally measured Tafel slopes for $O_2$ reduction in acid [39,40]. For negligible ohmic potential drop in both the electronic (solid-matrix) and ionic (polymer electrolyte) conductive phases of the catalyst layer, the overpotential in Eq. (17) is constant across the catalyst layer thickness [4,32].

The dimensionless number $\pi_9$ (Table 2) compares the intrinsic kinetic rate of the electrode reaction with the effective rate of $O_2$ diffusion in the catalyst layer (Eq. (18)). Therefore, $\pi_9$ could be considered the electrode kinetic equivalent of the second Damköhler number $Da_{II}$ (for a review see [22]). A low $Da_{II}$ in the present case means that the effective $O_2$ diffusion rate is high across the catalyst layer thickness compared to the intrinsic electrode kinetic rate defined at $E^0$ (note the $k^0$ in Eq. (18)).

Furthermore, it is easily recognized that the square root of $\pi_9$ is similar to the expression of the Thiele modulus $\phi$ for first-order kinetics [45]:

$$\pi_9 \equiv Da_{II} = \frac{(a_c k^0) Z_c^2}{D_{O_2,c}} = \phi^2, \tag{18}$$

where $a_c$ is the specific surface area of the catalyst layer, $D_{O_2,c}$ the effective $O_2$ diffusion coefficient in the catalyst layer, $k^0$ the standard heterogeneous rate constant and $Z_c$ the catalyst layer thickness.

The Thiele modulus as defined by Eq. (18) is related to the standard heterogeneous rate constant. However, it is important to consider also the electrode potential dependency by employing the product $\pi_9\pi_0$. Thus, from Eqs. (17) and (18) an overpotential-dependent Thiele modulus $\phi_E$ can be defined as

$$\pi_9\pi_0 = \phi_E^2 = \frac{(a_c k^0) Z_c^2}{D_{O_2,c}} \exp\left(-\frac{2.3}{b}\eta\right) = Da_{II} \exp\left(-\frac{2.3}{b}\eta\right). \tag{19}$$

The electrode potential-dependent Thiele modulus $\phi_E = \sqrt{\pi_9\pi_0}$, reflects the catalyst layer utilization efficiency and penetration depth. It must be noted that Perry, Newman and Cairns in the analysis of liquid-electrolyte fuel cells, introduced a Thiele modulus conceptually similar to $\phi_E$ but expressed in terms of the porous catalyst agglomerate radius instead of $Z_c$ [46]. The variant given in the present work, on the other hand, is based on the pseudohomogeneous film model of the catalyst layer.

From Eq. (18) for $Z_c = \text{const.}$, the higher $\phi$ or $Da_{II}$ the smaller the penetration depth of the $O_2$ reduction front inside the catalyst layer. Furthermore, from Eq. (19), for the same $Da_{II}$ the more negative the cathode overpotential, the higher $\phi_E$ and consequently, the lower the penetration depth of the reaction front. For efficient utilization of the Pt-based catalysts the physical thickness of the catalyst layer $Z_c$ should be approximately equal to the penetration depth $\nu_p$ given by the

following equations:

$$\nu_{\mathrm{p}} = \frac{Z_{\mathrm{c}}}{\phi} = \left(\frac{D_{\mathrm{O_2,c}}}{a_{\mathrm{c}}k^0}\right)^{1/2}, \tag{20}$$

$$\nu_{\mathrm{p,E}} = \frac{Z_{\mathrm{c}}}{\phi_{\mathrm{E}}} = \left(\frac{D_{\mathrm{O_2,c}}}{a_{\mathrm{c}}k^0}\right)^{1/2} \exp\left(\frac{2.3}{2b}\eta\right). \tag{21}$$

Eqs. (20) and (21) define the penetration depth in terms of electrode kinetics coupled with $O_2$ mass transport based on the pseudohomogeneous film model. Newman and Tiedemann defined a porous electrode penetration depth for the case of electrode kinetics in conjunction with ohmic limitation [24]. Their ratio was also inversely proportional to the square root of the specific surface area–exchange current density product $a_{\mathrm{c}}i_0$.

The rest of the dimensionless numbers in Table 2, i.e. from $\pi_{10}$ to $\pi_{17}$, can be related to dimensionless numbers that have already been introduced. Thus, $\pi_{10}$ (Eq. (22)) could be considered the Nusselt number for $O_2$ transport in the catalyst layer (see also Eq. (8) and Ref. [32]), assuming diffusion across the entire catalyst layer thickness and fast electrode reaction concentrated at catalyst layer/bulk membrane-electrolyte interface (Fig. 1) with $\Delta C_{\mathrm{O_2,c}} = C_{\mathrm{O_2},1} - C_{\mathrm{O_2},2}$, where $C_{\mathrm{O_2},2} = 0$ and $\Delta C_{\mathrm{O_2}} = C_{\mathrm{O_2},1} = C_{\mathrm{O_2}}$:

$$\pi_{10} = \frac{iZ_{\mathrm{c}}s_{\mathrm{O_2}}}{nFD_{\mathrm{O_2,c}}C_{\mathrm{O_2}}} = \frac{i}{i_{\mathrm{L,O_2,c}}}. \tag{22}$$

The concentration $C_{\mathrm{O_2}}$, corresponding to the catalyst/gas-diffusion layer interface, can be calculated from Henry's law: $C_{\mathrm{O_2},1} = x_{\mathrm{O_2},1}p_{\mathrm{d}}/H$ with $p_{\mathrm{d}}$ the inlet air pressure in the diffuser, $x_{\mathrm{O_2},1}$ the $O_2$ mole fraction at the catalyst/gas-diffusion layer interface and $H$ is Henry's law constant [4].

The numbers $\pi_{14}$ and $\pi_{15}$ on the other hand, express the ohmic drop in the membrane-electrolyte $\Delta\Phi$ and solid phases $\Delta\Phi_{\mathrm{s}}$ of the catalyst layer, respectively, similarly to $\pi_5$ but taking into account the effective values in the porous media of the respective physico-chemical constants, $k_{\Phi,\mathrm{c}}$ and $k_{\mathrm{p,c}}$.

The dimensionless numbers $\pi_{16}$ and $\pi_{17}$ are similar to $\pi_6$ (Table 1). Thus, $\pi_{16}$ and $\pi_{17}$ compare the effective ionic $\kappa_{\mathrm{c}}$ and electronic $\sigma_{\mathrm{c}}$ conductivities, respectively, with the surface-convective proton conductivity of the membrane-electrolyte:

$$\pi_{16} = \frac{\kappa_{\mathrm{c}}\mu s_{\mathrm{O_2}}^2}{(n|z_{\mathrm{f}}|FC_{\mathrm{f}})^2 Z_{\mathrm{c}}^2} = \frac{\kappa_{\mathrm{c}}\mu}{\left(\frac{n}{s_{\mathrm{O_2}}}\right)^2 q_{\mathrm{f}}^2} \tag{23}$$

and

$$\pi_{17} = \frac{\sigma_{\mathrm{c}}\mu s_{\mathrm{O_2}}^2}{(n|z_{\mathrm{f}}|FC_{\mathrm{f}})^2 Z_{\mathrm{c}}^2} = \frac{\sigma_{\mathrm{c}}\mu}{\left(\frac{n}{s_{\mathrm{O_2}}}\right)^2 q_{\mathrm{f}}^2}. \tag{24}$$

Regarding the polarization behaviour of the catalyst layer, the following operating regimes can be identified [46]: (I) intrinsic electrode kinetic control, (II) mixed; electrode kinetics and $O_2$ mass transport control, (III) kinetics coupled with ionic transport (i.e. ionic conductivity effect) and (IV) electrode kinetics, $O_2$ and ionic transport control. It is proposed that the catalyst layer polarization curves corresponding to the various operating regimes can be described in a dimensionless form using a monomial correlating function and $\phi_{\mathrm{E}}^2$ as the dependent variable:

$$\phi_{\mathrm{E}}^2 = y_{0,\mathrm{c}}\pi_{10}^{y_{10}}\pi_{16}^{y_{16}}\pi_{12}^{y_{12}}, \tag{25}$$

or explicitly,

$$\frac{(a_{\mathrm{c}}k^0)Z_{\mathrm{c}}^2}{D_{\mathrm{O_2,c}}}\exp\left(-\frac{2.3}{b}\eta\right) = y_{0,\mathrm{c}}\left(\frac{iZ_{\mathrm{c}}s_{\mathrm{O_2}}}{nFD_{\mathrm{O_2,c}}C_{\mathrm{O_2}}}\right)^{y_{10}}\left(\frac{\kappa_{\mathrm{c}}\mu s_{\mathrm{O_2}}^2}{(n|z_{\mathrm{f}}|FC_{\mathrm{f}})^2 Z_{\mathrm{c}}^2}\right)^{y_{16}} \times \left(\frac{|z_{\mathrm{f}}|\,C_{\mathrm{f}}}{C_{\mathrm{O_2}}}\right)^{y_{12}}. \tag{26}$$

To reduce the number of unknown exponents, $\pi_{16}$ and $\pi_{12}$ could be combined in one term, $\pi_{16,\mathrm{C}}$, considering $y_{12} = 2y_{16}$, which leads to the following equations:

$$\phi_{\mathrm{E}}^2 = y_{0,\mathrm{c}}\pi_{10}^{y_{10}}\pi_{16,\mathrm{C}}^{y_{16}} \tag{27}$$

and

$$\frac{(a_{\mathrm{c}}k^0)Z_{\mathrm{c}}^2}{D_{\mathrm{O_2,c}}}\exp\left(-\frac{2.3}{b}\eta\right) = y_{0,\mathrm{c}}\left(\frac{iZ_{\mathrm{c}}s_{\mathrm{O_2}}}{nFD_{\mathrm{O_2,c}}C_{\mathrm{O_2}}}\right)^{y_{10}}\left(\frac{\kappa_{\mathrm{c}}\mu s_{\mathrm{O_2}}^2}{(nFC_{\mathrm{O_2}})^2 Z_{\mathrm{c}}^2}\right)^{y_{16}}. \tag{28}$$

For regime I: intrinsic electrode kinetic control, the effective $O_2$ diffusivity and ionic (i.e. proton) conductivity do not affect the performance, therefore, in Eqs. (27) and (28) simply $y_{16} = 0$ while $y_{10} = 1$, with $y_{0,\mathrm{c}} = 1$ one obtains:

$$\phi_{\mathrm{E}}^2 = \pi_{10} \tag{29}$$

and

$$i = \frac{n}{s_{\mathrm{O_2}}}FZ_{\mathrm{c}}a_{\mathrm{c}}k^0C_{\mathrm{O_2}}\exp\left(-\frac{2.3}{b}\eta\right). \tag{30}$$

Moreover, $y_{10}$ was also determined from a fit of $\eta$ as a function of $\ln i$, with the slope equal to $-y_{10}b/2.3$ from Eq. (29) written as $\phi_{\mathrm{E}}^2 = \pi_{10}^{y_{10}}$. The experimental cathode polarization curve at 5 atm neat $O_2$ pressure reported by Springer et al. (Fig. 15, curve a, in Ref. [40]) was employed. For the current density range of 740–8000 A m$^{-2}$, using $b = 0.085$ V dec$^{-1}$ [40], it was found that $y_{10} = 1$, confirming, therefore, the dependence expressed by Eqs. (29) and (30).

In the case of mixed control according to regime II: electrode kinetics coupled with $O_2$ transport, using $y_{16} = 0$ and $y_{0,\mathrm{c}} = 1$, the general equation is

$$\phi_{\mathrm{E}}^2 = \pi_{10}^{y_{10}} \tag{31}$$

or

$$i = \frac{n}{s_{O_2}} F C_{O_2} Z_c^{((2/y_{10})-1)} (a_c k^0)^{1/y_{10}} \times (D_{O_2,c})^{(1-(1/y_{10}))} \exp\left(-\frac{2.3}{y_{10} b}\eta\right). \quad (32)$$

The general equation for regime II (i.e., Eq. (32)) shows the characteristic multiple Tafel slope behaviour of the porous electrode:

$$b^* = y_{10} b. \quad (33)$$

Eqs. (31) and (32) show the power of dimensional analysis to provide in a mathematically simple way a general analytical solution to a complex problem. Employing the experimental cathode polarization curve obtained by Springer and coworkers at 5 atm air pressure (Fig. 15, curve b, in Ref. [40]), $y_{10}$ was determined from a fit to Eq. (31), as described previously. Using the current density range of 3000–9100 A m$^{-2}$, yielded $y_{10} = 2$. Thus, according to Eq. (33) a double Tafel slope was obtained for the catalyst layer operating on 5 atm air, i.e. $b^* = 2b$. The same Tafel slope was also obtained using the data for 2 atm $O_2/N_2$ mixture with 13.5 vol.% $O_2$ for current densities up to 5000 A m$^{-2}$ [40]. Eq. (32) in the case of $y_{10} = 2$ becomes

$$i = \frac{n}{s_{O_2}} F C_{O_2} (a_c k^0 D_{O_2,c})^{1/2} \exp\left(-\frac{2.3}{2b}\eta\right). \quad (34)$$

Using an asymptotic approach [47], Perry et al. derived equations for the catalyst layer under kinetic and mixed, kinetic and $O_2$ mass transport control, respectively, similar to Eqs. (30) and (34) (i.e. particular case of $y_{10} = 2$) [46]. Comparing Eqs. (30) and (34) the double Tafel slope is indicative of mass transfer effects limiting the current density, while for both cases the oxygen concentration dependence is of first order.

In addition to kinetics and $O_2$ mass transfer, the ionic conductivity could affect the performance of the catalyst layer. Experimental results [40] indicated that current ratio measured at 0.7 V between the runs with 5 atm air and 2 atm $O_2/N_2$ mixture with 13.5% $O_2$, was around 2 instead of about 5, what would have been expected based on the first-order $O_2$ partial pressure dependence (Eq. (34)). This limitation was attributed to ionic conductivity effects [40]. The latter could be accommodated by using the ionic conductivity term in Eqs. (27) and (28) and determining $y_{16}$ in addition to the $O_2$ mass transfer effect characterized by $y_{10} = 2$ as shown before. Thus, based on Eq. (28) with $y_{10} = 2$, the current density is proportional to the $O_2$ concentration according to:

$$i \sim C_{O_2}^{y_{16}+1}. \quad (35)$$

Substituting in Eq. (35) the cathode current densities measured at 0.7 V (Fig. 15, Ref. [40]), i.e., 11,500 A m$^{-2}$ for 5 atm air and 6000 A m$^{-2}$ for 2 atm $O_2/N_2$ mixture with 13.5% $O_2$,

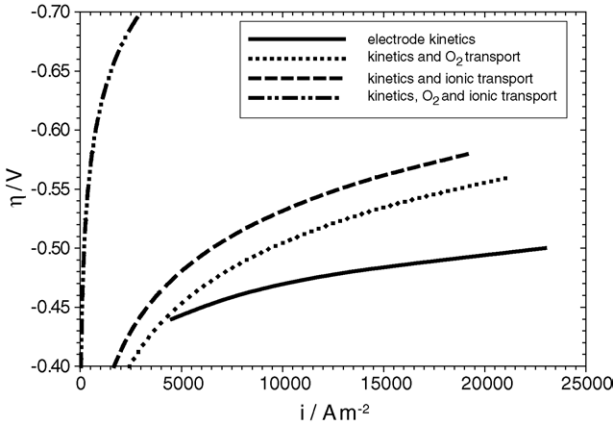


Fig. 4. Catalyst layer: overpotential as a function of current density for various oxygen reduction rate-limiting scenarios. Summary of conditions: $Z_c = 10\ \mu m$, $\kappa_c = 0.25\ S\ m^{-1}$, $b = 0.085\ V\ dec^{-1}$, $a_c = 2 \times 10^7\ m^2\ m^{-3}$, $D_{O_2,c} = 2 \times 10^{-8}\ m^2\ s^{-1}$, $T = 353\ K$.

a half-order $O_2$ concentration dependence of the current density is obtained. Hence $y_{16} = -0.5$ and Eq. (27) becomes

$$\phi_E^2 = \pi_{10}^2 \pi_{16,C}^{-1/2}. \quad (36)$$

From Eq. (36) the polarization equation in the case of combined ionic and $O_2$ mass transport control coupled with electrode kinetics is

$$i = \sqrt{\frac{n}{s_{O_2}} F a_c k^0 D_{O_2,c} \frac{C_{O_2}}{Z_c} (\kappa_c \mu)^{1/2}} \exp\left(-\frac{2.3}{2b}\eta\right). \quad (37)$$

To the knowledge of the author equations (36) and (37) are the first analytical equations describing the proton transport effect combined with kinetics and $O_2$ transport (regime IV). The current density shows a half-order dependence on the $O_2$ concentration as observed experimentally [40]. Moreover, Eq. (37) gives a 1/4-order dependence of $i$ on $\kappa_c$, which predicts fairly well the current density ratios reported by Springer et al., corresponding to 0.7 V cathode potential and effective ionic conductivities of the catalyst layer, of 0.5, 0.2 and 0.08 S m$^{-1}$ (Fig. 7 in Ref. [40]).

Eq. (37) shows that in the case of both $O_2$ and ionic transport limitation, the current density is inversely proportional with the square root of catalyst layer thickness for a constant catalyst specific surface area $a_c$. Therefore, a thin catalyst layer is required to reduce the impact of the limiting transport steps. Finally, Eq. (37) with $\eta$ constant across the catalyst layer thickness implies that the ionic conductivity effect reflects not an ohmic control but a proton reactant (Eq. (2)) diffusion limitation.

Fig. 4 compares the effects of the various limiting factors on the catalyst layer polarization behaviour for 5 atm air at 353 K according to Eqs. (30), (34) and (37), respectively, assuming no gas diffusion-backing layer limitation. The physico-chemical parameters were: $Z_c = 10\ \mu m$, $\kappa_c = 0.25\ S\ m^{-1}$, $b = 0.085\ V\ dec^{-1}$ [40], $a_c = 2 \times 10^7\ m^2\ m^{-3}$, $D_{O_2,c} = 2 \times 10^{-8}\ m^2\ s^{-1}$ [39]

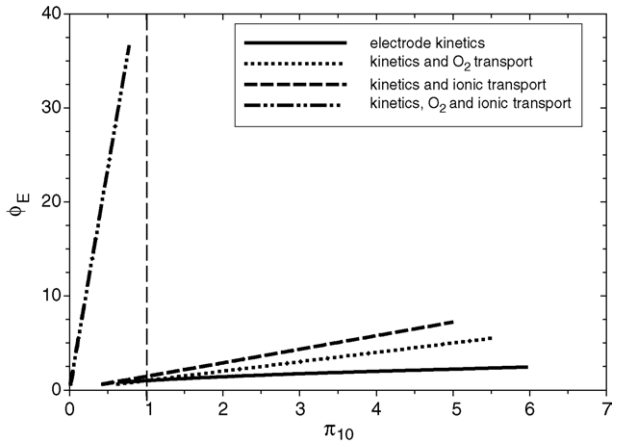


Fig. 5. Catalyst layer: Thiele modulus for electrode kinetics $\phi_E$ as a function of $\pi_{10}$. Conditions identical to Fig. 4.

and $C_{O_2} = 4.96\,\text{mol}\,\text{m}^{-3}$ corresponding to 5 atm air and Henry's constant of $2.04 \times 10^4\,\text{Pa}\,\text{m}^3\,\text{mol}^{-1}$ calculated from the formulae given by Bernardi and Verbrugge [4] for the $O_2$ solubility in Nafion. The standard heterogeneous rate constant $k^0$ was $7.9 \times 10^{-11}\,\text{m}\,\text{s}^{-1}$, calculated from Eq. (3) using $i_0 = 1.5 \times 10^{-4}\,\text{A}\,\text{m}^{-2}$ and $C_{O_2,\text{ref}} = 4.9\,\text{mol}\,\text{m}^{-3}$ for 1 bar $O_2$ pressure [39].

Additionally, the combined influence of electrode kinetics and ohmic drop (i.e. assuming fast $O_2$ transport) was plotted using the equation derived by Perry et al. based on asymptotic analysis [46]:

$$i = \sqrt{\frac{2n_{O_2} Fa_c k^0 C_{O_2} \kappa_c b}{2.3}} \exp\left(-\frac{2.3}{2b}\eta\right). \tag{38}$$

Fig. 5 on the other hand, shows the same effects as Fig. 4 but expressed in dimensionless form as the dependence of the overpotential-dependent Thiele modulus $\phi_E$ as a function of the $O_2$ Nusselt number for the catalyst layer, $\pi_{10}$.

As shown in Fig. 4, superficial current densities up to $23{,}000\,\text{A}\,\text{m}^{-2}$ could be achieved in the case of intrinsic electrode kinetic control (Eq. (26)) with cathode overpotentials $-\eta \leq 0.5$ V. Both $O_2$ and proton transport limitations, separately and in combination, have the role of increasing the overpotential required for a given superficial current density. The combined limiting effect of $O_2$ and ionic transport increases dramatically the cathode overpotential, e.g. a current density of about $3000\,\text{A}\,\text{m}^{-2}$ was obtained at an overpotential of $-0.7$ V (Fig. 4). In dimensionless form, Fig. 5 shows that at constant $\pi_{10}$ the overpotential-dependent Thiele modulus was much higher when both ionic and $O_2$ transport limited the electrode performance.

The penetration depth $\nu_{p,E}$ according to Eq. (21) at $\pi_{10} = 0.6$ (i.e. $2300\,\text{A}\,\text{m}^{-2}$) was about 15 μm for $O_2$ transport limitation and 0.4 μm for both ionic and $O_2$ transport control. This result shows clearly the inefficient utilization of the catalyst layer thickness in the latter scenario (physical thickness of 10 μm).

Based on Fig. 5 the parameter $\tau = \frac{\Delta\phi_E}{\Delta\pi_{10}}$ could serve as an indicator for the different operating regimes:

- Regime I: intrinsic electrode kinetics $\tau < 1$,
- Regime II: electrode kinetic and $O_2$ mass transport $\tau = 1$,
- Regime III: electrode kinetic and ionic transport $\tau > 1$, and
- Regime IV: electrode kinetics with $O_2$ and ionic transport $\tau \gg 1$.

The ohmic potential drop in both the electrolyte and electronic conductor phases of the catalyst layer can be expressed with the dimensionless ratios given in Table 2. For the electrolyte phase the correlating function is similar to the one described for the bulk electrolyte-membrane (see Section 4.1) but in the expression of the dimensionless ratios the effective values of the physico-chemical parameters are used. In the case of the electronic conductor solid phase, Ohm's law in dimensionless form is written as: $\pi_{15} = \pi_{10}\pi_8^{-1}\pi_{12}^{-1}\pi_{13}^{-1}\pi_{17}^{-1}$. Furthermore, depending on the effective conductivities of the two phases $\sigma_c$ and $\kappa_c$, the ohmic potential drop for the electrolyte and/or solid phase can be included in the total polarization behaviour of the catalyst layer [24,46]. One way to evaluate the importance of the ohmic drop is to compare the charge-transfer and ohmic resistances by calculating the Wagner numbers for the catalyst layer, $Wa = \kappa_c(\delta\eta/\delta i)/Z_c$ and $Wa_s = \sigma_c(\delta\eta/\delta i)/Z_c$, using the polarization expressions given by Eqs. (30), (34) and (37). For $Wa$, $Wa_s < 1$ the ohmic resistance dominates and it must be accounted for in the polarization equation.

### 4.3. Dimensionless numbers and monomial correlating equations for the gas-diffusion (backing) layer

Table 3 shows the dimensionless numbers derived for the gas-diffusion layer using the Quraishi–Fahidy technique. One goal for the gas-diffusion layer analysis is to evaluate the effect of mass transport on the $O_2$ mole fraction at the catalyst/gas diffusion-backing layer interface, $x_{O_2,1}$ (see Fig. 1). Therefore, in Table 3 the $O_2$ mole fraction difference across the diffuser has been employed, $\Delta x_{O_2} = x_{O_2,0} - x_{O_2,1}$, where $x_{O_2,0}$ is the inlet $O_2$ mole fraction.

Relevant mass and momentum transport related dimensionless numbers characteristic for the gas-diffusion layer are (Table 3): Schmidt numbers for the effective binary mixture diffusivities of $O_2$–$N_2$ $\pi_{18}$, and water–air $\pi_{19}$, respectively, the water Reynolds number in the diffuser $\pi_{22}$, and the Nusselt number for $O_2$ mass transfer in the gas diffusion layer $\pi_{23}$ or $\pi_{23,w}$ (see also Eq. (8)):

$$\pi_{23} = \frac{i_s s_{O_2} Z_d RT}{nFD_{N_2-O_2,d}\Delta x_{O_2} p_d} = Nu_{E,d}, \tag{39}$$

$$\pi_{23,w} = \frac{i_s s_{O_2} Z_d RT}{nFD_{w-air,d}\Delta x_{O_2} p_d} = Nu_{E,d,w}, \tag{40}$$

where $p_d$ is the inlet air pressure at the cathode diffuser, $D_{N_2-O_2,d}$ the effective binary $O_2$–$N_2$ diffusivity (a function of wet-proofed pore volume fraction), $D_{w-air,d}$ the effective water–air binary diffusivity (a function of the total pore volume fraction in the absence of wet-proofing), $i_s$ the superficial current density in the diffuser solid phase (equal to the operating current density $i_t$) and $Z_d$ the diffusion layer thickness.

Eqs. (39) and (40) are based on the pseudohomogeneous film model considering that the electrochemical reaction is concentrated at the catalyst/gas-diffusion layer interface (position 1, Fig. 1). Moreover, Eqs. (39) and (40) distinguish between two scenarios as suggested by the respective diffusivities. Eq. (39) considers a separate network of hydrophobic and hydrophilic pores in the diffuser (realized in practice by addition of a wet-proofing agent such as PTFE) and consequently, air diffuses exclusively through the hydrophobic pore network. While Eq. (40), by employing $D_{w-air,d}$ inherently implies that air and water share the same network of pores.

The mass transfer limiting condition in Eqs. (39) and (40) is given by $x_{O_2,1} = 0$ (i.e., the $O_2$ is completely consumed by fast electrode reaction at the catalyst/gas-diffusion layer interface). This leads to

$$\pi_{23,L} = \frac{i_s s_{O_2} Z_d RT}{nFD_{N_2-O_2,d} x_{O_2,0} p_d} = \frac{i_s}{i_{L,O_2,d}} \tag{41}$$

and

$$\pi_{23,L,w} = \frac{i_s s_{O_2} Z_d RT}{nFD_{w-air,d} x_{O_2,0} p_d} = \frac{i_s}{i_{L,O_2,d,w}}, \tag{42}$$

where $i_{L,O_2,d}$, and $i_{L,O_2,d,w}$ are the gas diffuser mass transfer limited superficial current densities without and with interference from a co-diffusing water phase, respectively.

A monomial correlating equation for the case of shared pore network can be written as

$$\pi_{23,w} = y_{0,d}\pi_{22}^{y_{22}} \text{ i.e., } Nu_{E,d,w} = y_{0,d}\, Re_w^{y_{22}}. \tag{43}$$

A high $Re_w$ in the diffuser describing water flow from the catalyst layer into the gas diffusion layer (i.e., flooding) impedes the $O_2$ gas transport and reduces $Nu_{E,d,w}$ in other words, $\Delta x_{O_2} = x_{O_2,0} - x_{O_2,1}$ increases. Therefore, $y_{22} < 0$ in the case of backing-diffusion layer flooding.

Substituting the corresponding dimensionless ratios in Eq. (43) gives $x_{O_2,1}$ in the scenario of shared pore network for both air and water:

$$\frac{x_{O_2,1}}{x_{O_2,0}} = 1 - \frac{1}{y_{0,d}} \left( \frac{i_s s_{O_2} Z_d RT}{nFD_{w-air,d} x_{O_2,0} p_d} \right) \left( \frac{v_{0,d} \rho Z_d}{\mu} \right)^{-y_{22}}$$

$$= 1 - \frac{1}{y_{0,d}} \pi_{23,L,w}\, Re_w^{y_{22}}. \tag{44}$$

As an example, using the superficial water velocities reported by Bernardi and Verbrugge at 4000 and 6000 A m$^{-2}$ (Fig. 9, Ref. [5]) and assuming $\Delta x_{O_2} = 0.05 x_{O_2,0}$ for the former and $\Delta x_{O_2} = 0.1 x_{O_2,0}$ for the latter superficial current density, Eq. (44) yields $y_{22} = -0.45$ and $y_{0,d} = 10$.

In the case of separate hydrophobic and hydrophilic pore networks in the diffuser maintained throughout the operation of the fuel cell, Eq. (44) reduces to

$$\frac{x_{O_2,1}}{x_{O_2,0}} = 1 - \frac{1}{y_{0,d}} \pi_{23,L} = 1 - \frac{1}{y_{0,d}} \frac{i_s}{i_{L,O_2,d}}. \tag{45}$$

Substituting the mole fraction ratios for 1000, 5000 and 8000 A m$^{-2}$ from Fig. 7 of Ref. [4], yields $y_{0,d} \cong 1$. Thus, Eq. (45) is consistent with the familiar form of the surface concentration obtained using Fick's law.

The ohmic potential drop in the solid electronic conductor phase can be expressed in a dimensionless form as

$$\pi_{24} = y'_{0,d} \pi_{18}^{y_{18}} \pi_{22}^{y_{22}} \pi_{23}^{y_{23}} \pi_{25}^{y_{25}}, \tag{46}$$

where $y'_{0,d} = 1$, $y_{23} = 1$ and $y_{18} = y_{22} = y_{25} = -1$, yields the expression for Ohm's law.

### 4.4. Applications

Sensitivity analysis is performed on the developed correlating equations with respect to key variables and exponents such as $y_{10}$ in Eq. (32) controlling the multiple-Tafel slope value of the mixed: kinetic and $O_2$ mass transfer regime, $y_{22}$ in Eq. (43) indicative of diffusion-backing layer flooding and the combined influence of catalyst layer thickness and effective conductivity on regime IV (Eq. (37)). Furthermore, the dimensional analysis-based model predictions including the membrane ohmic drop described by Eq. (13), are compared with experimental data independent of the those used to develop these correlations.

Fig. 6 shows the effect of $y_{10}$ on the cathode potential $E_{oc} + \eta$ for air pressure of 5 atm, at 353 K. It was assumed that the open-circuit value $E_{oc} = 0.98$ V due to the establishment of a mixed potential on the cathode surface. A separate hydrophilic–hydrophobic pore network was considered in the diffuser expressed by Eq. (45) (i.e. no gas diffuser flooding limitation). The catalyst layer thickness was 25 μm and the specific surface area of the catalyst $2 \times 10^9$ m$^2$ m$^{-3}$. The rest

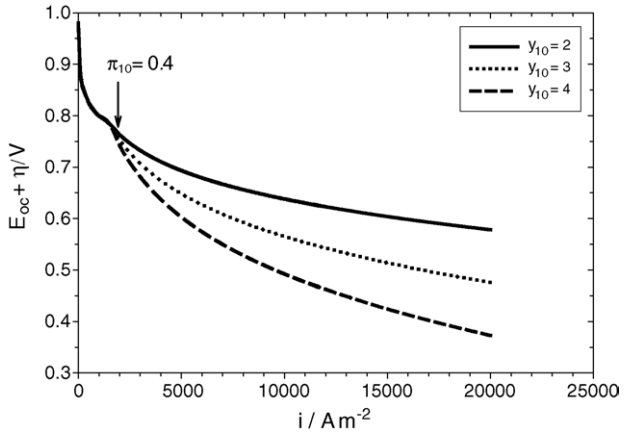


Fig. 6. Effect of parameter $y_{10}$ on the catalyst layer polarization under mixed, electrode kinetic and $O_2$ mass transfer control. 5 atm air pressure, 353 K.

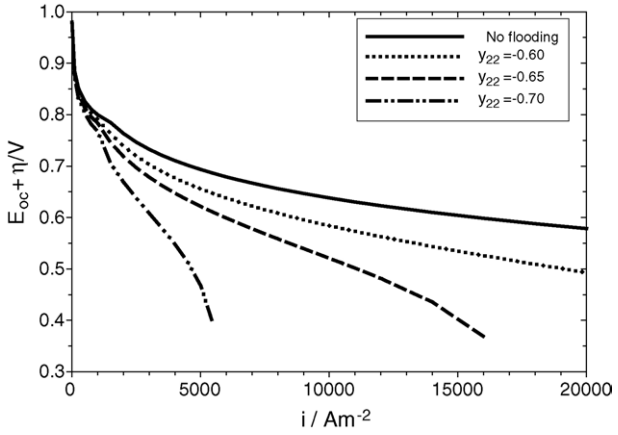


Fig. 7. Effect of diffuser flooding on the catalyst layer polarization under mixed, electrode kinetic and $O_2$ mass transfer control with $y_{10} = 2$. 5 atm air pressure, 353 K.

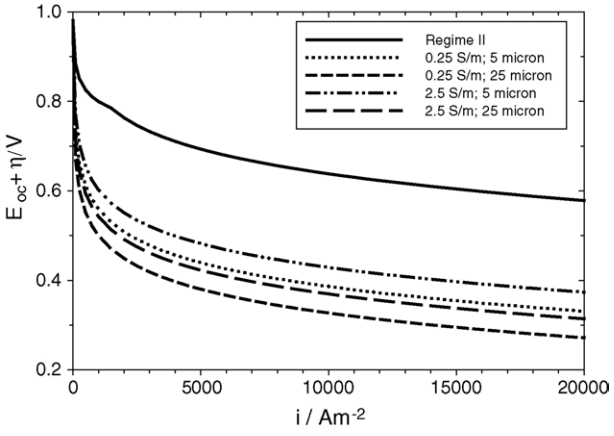


Fig. 8. Comparison between regime II (kinetic and $O_2$ mass transfer control) and regime IV (kinetic, $O_2$ and ionic mass transfer limitation) for catalyst layer polarization. 5 atm air pressure, 353 K, catalyst layer thickness: 5 and 25 μm, effective ionic conductivity of the catalyst layer 0.25 and 2.5 S m$^{-1}$.

of the physico-chemical data was given in Section 4.2. The dimensionless number $\pi_{10}$ could serve as an indicator of intrinsic kinetic or mixed (kinetic and $O_2$ transport) control. Under the conditions of Fig. 6, Eqs. (30) for kinetic and (32) for mixed control (regime II), respectively, intersect at $\pi_{10} = 0.4$. Regime II dominates at $\pi_{10} > 0.4$ with $y_{10}$ (multiple-Tafel slope value) affecting the polarization behaviour, whilst for $\pi_{10} \leq 0.4$ the polarization behaviour is described by regime I (i.e. intrinsic electrode kinetic control). Fig. 6 shows that the transition between the two regimes occurred at 1500 A m$^{-2}$.

In regime II the $O_2$ penetration depth becomes smaller than the physical thickness of the catalyst layer. In other words, the $y_{10}$ effect is a reflection of the different oxygen permeabilities of the catalyst layer.

Fig. 7 shows the effect of diffuser flooding on the polarization behaviour using Eq. (44) to calculate the $O_2$ concentration at the diffuser/catalyst layer interface. Three $y_{22}$ values were compared, −0.6, −0.65 and −0.7, respectively, whilst $y_{0,d} = 10$ (Section 4.3) and $y_{10} = 2$. The diffuser thickness was 260 μm. The rest of the physico-chemical parameters were the same as presented previously. Fig. 7 reveals that the diffuser flooding can be succinctly described by Eqs. (43) and (44) coupled with Eq. (32) for regime II. Thus, the proposed monomial correlations eliminate the need for the exponential term used previously in the literature to model empirically the $O_2$ mass transfer (Eq. (1)) [18]. The more negative $y_{22}$ the more severe the diffuser-backing layer flooding, compromising the cathode performance. Under the conditions explored in Fig. 7 at 5000 A m$^{-2}$ the cathode potential in the absence of flooding (i.e. separate hydrophilic and hydrophobic pore network) was 0.67 V, while 0.62 and 0.47 V were obtained in the case of flooding characterized by $y_{22} = -0.65$ and −0.7, respectively (Fig. 7).

The proton transport influence on the cathode polarization behaviour can be detected by the combined effect of the catalyst layer thickness $Z_c$ and specific protonic conductivity $\kappa_c$. Assuming $y_{10} = 2$, Eq. (37) shows that in the case of both ionic and $O_2$ transport limitation (regime IV) for a given overpotential the current density is proportional to the square root of the catalyst layer thickness, whilst for intrinsic $O_2$ mass transport control (Eq. (34), regime II), the polarization behaviour is independent of thickness. Fig. 8 compares the two polarization regimes II and IV, in the case of 5 and 25 μm catalyst layer thickness and 0.25–2.5 S m$^{-1}$ protonic conductivity, respectively. It was assumed that the cathode is not limited by diffuser flooding and the specific catalyst surface area is the same in all cases. Under the conditions of Fig. 8, the combined limitation of proton and $O_2$ transport in the catalyst layer decreases the cathode potential between about 0.2 and 0.6 V at current densities above 1000 A m$^{-2}$. Based on Fig. 8, a 10 times decrease of $\kappa_c$ and a 5 times increase of $Z_c$ lower the cathode potential by approximately the same amount. Thus, the relative effect of the catalyst layer thickness is higher compared to the protonic conductivity.

Lastly, the effect of membrane ohmic loss as described by Eq. (13) is analyzed in addition to the cathode polarization behaviour, by comparison with recently obtained experimental data. The polarization curves for a 25 cm$^2$ active geometric area fuel cell composed of Toray carbon paper gas diffusion layer, 0.5 mg cm$^{-2}$ Pt load (i.e. 20 wt.% Pt on Vulcan XC-72) and Nafion 115 were recorded at 353 K and 2.5 atm pressure on both air and $H_2$ side under two conditions: un-hydrated new MEA and conditioned (i.e. fully hydrated) MEA. The MEA conditioning was achieved by running the cell in galvanostatic mode at three different loads until the cell voltage drift was below 1 mV per hour for two consecutive hours [48].

The goal was to evaluate whether the developed correlating equations could predict the single-cell behaviour under two significantly different operating conditions. As expected the performance of the unconditioned MEA was poor, for example at 7000 A m$^{-2}$ the cell voltage was about 0.3 V, whilst the fully hydrated MEA at the same current density gave 0.57 V (Fig. 9). For both cases the modeling equations resulting from dimensional analysis showed a good fit with

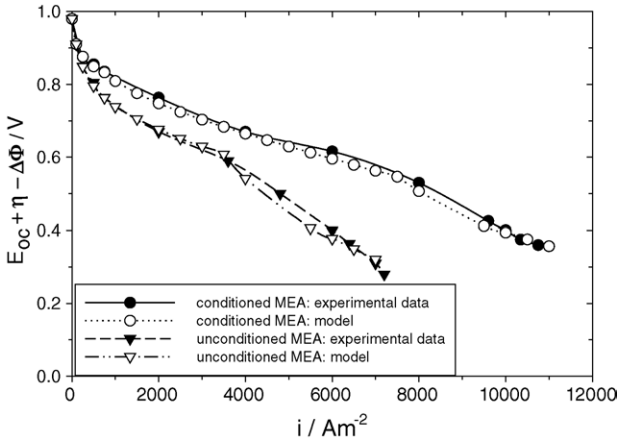


Fig. 9. Comparison between experimental data and model prediction based on correlating equations among dimensionless numbers for conditioned and unconditioned MEA operated at 2.5 atm air and $H_2$ pressure, 353 K.

the experimental data (Fig. 9). It must be noted that in the model the contribution of the $H_2$ oxidation overpotential was neglected for the sake of simplicity.

The conditioned MEA results (Fig. 9) were modeled by coupling the membrane ohmic drop given by Eq. (16) with $y_4 = -1$ (i.e. no hydrostatic pressure difference effect) with the following catalyst layer polarization models: intrinsic kinetic control (Eq. (30) with $i_0 = 6 \times 10^{-4}$ A m$^{-2}$ and $b = 0.085$ V) up to 750 A m$^{-2}$, and mixed, kinetic and mass transfer control expressed by Eq. (32) with $y_{10} = 2$, without gas diffuser flooding for $9500 \geq i \geq 750$ A m$^{-2}$ and with gas diffuser flooding (Eq. (44), $y_{22} = -0.65$ and $y_{0,d} = 30$) for $i \geq 10{,}000$ A m$^{-2}$. The abrupt voltage drop in the case of the unconditioned MEA on the other hand, could be described by the previously employed membrane ohmic drop equation (16) in conjunction with the regime III catalyst layer polarization equation (38) expressing mixed kinetic and ohmic drop limitation ($\kappa_c = 4$ S m$^{-1}$), coupled with diffuser flooding for $i \geq 4000$ A m$^{-2}$. Thus, it could be concluded that the correlations among dimensionless numbers could lead to practically useful models of the MEA performance and moreover, they could offer insights into the phenomena responsible for the polarization behaviour without increased mathematical complexity.

## 5. Conclusions

The Quraishi–Fahidy dimensional analysis technique was employed to derive characteristic dimensionless numbers for the membrane-gas diffusion electrode assembly in polymer electrolyte fuel cells. It was shown for the first time that monomial correlating functions among dimensionless ratios could be used to describe concisely and in an easy to use form, the non-linear dependence of the membrane ohmic drop as a function of operating conditions (Eq. (12)), the polarization behaviour of the catalyst layer under combinations of electrode kinetics, oxygen and/or ionic transport limitations (Eq. (25)) and the mass transfer in the gas diffuser (Eqs. (44) and (45)). The dimensionless correlations were validated against experimental data and/or independent mathematical modeling results reported in the literature.

A dimensional analysis-based approach coupled with a mathematical model of the fuel cell systems could be useful to quantify and analyze new experimental data for a wide range of conditions by determining the exponents and coefficients $y_i$ in the corresponding monomial correlations. It is proposed that using representative single cells for a specific fuel cell stack development, a data bank of $y_i$ exponents/coefficients could be generated for a variety of operating conditions, by fitting the experimental data to the various correlating functions. In the case when $y_i$ is dependent on the employed range of the variables (e.g., low current density experiments yield a set of values different than those obtained at high current densities), interpolation of the dimensionless correlation could be performed according to the method developed by Churchill and Usagi [27]. The monomial correlations for the MEA in conjunction with the experimentally determined $y_i$ exponent/coefficient data bank could be easily implemented in more complex, design specific, mathematical models of the fuel cell stack.

Lastly, while the present dimensional analysis has been applied to the equations of the Bernardi–Verbrugge PEM fuel cell model, it is envisaged that a similar procedure could be employed for other models of the PEM fuel cell and for different fuel cell types such as solid oxide and molten carbonate.

## Acknowledgements

The financial support of the author's research by the British Columbia Advanced Systems Institute, the Natural Sciences and Engineering Research Council of Canada, and Western Economic Diversification of Canada are gratefully acknowledged.

## Appendix A. Membrane characteristics

Table A1 lists the physical properties and the ionic (fixed-negative charge-site) concentrations for the 1100 equivalent weight series Nafion (i.e., N112, NE1135, N115 and N117) and Dow membranes relevant to the present work.

The fixed charge-site concentration $C_f$ and the equivalent weight EW are given by the following equations:

$$C_f = \frac{AC}{|z_f|}\frac{BW}{Z_m} \tag{A.1}$$

and

$$\mathrm{EW} = \frac{1}{\mathrm{AC}}, \tag{A.2}$$

where AC is acid (or proton exchange) capacity ($\mathrm{eq\,kg^{-1}}$), BW the membrane basis weight ($\mathrm{kg\,m^{-2}}$) and $Z_m$ the wet membrane thickness (m).

The hydraulic and electrokinetic permeabilities of the membranes at 353–368 K were [5]: $k_p = 1.8 \times 10^{-18}\,\mathrm{m^2}$ for both Nafion and Dow, while $k_\Phi = 7.19 \times 10^{-20}\,\mathrm{m^2}$ for Nafion and $1.13 \times 10^{-19}\,\mathrm{m^2}$ for Dow membranes, respectively.

For N117 the membrane specific conductivities under open-circuit condition $\kappa_0$ for Figs. 2 and 3 were calculated employing $\lambda = 11$ and 16, respectively, in Eq. (11). Thus $\kappa_0$ is equal to $13.2\,\mathrm{S\,m^{-1}}$ for conditions relevant to Fig. 3 and $10.3\,\mathrm{S\,m^{-1}}$ for Fig. 2, respectively. For the rest of the Nafion membranes $\kappa_0$ was obtained by applying the thickness correction factors with respect to $\kappa_{0,\mathrm{N117}}$ derived from the work of Büchi and Scherer [34]:

$$\frac{\kappa_{0,\mathrm{N117}}}{\kappa_{0,\mathrm{N112}}} = 1.26, \qquad \frac{\kappa_{0,\mathrm{N117}}}{\kappa_{0,\mathrm{NE1135}}} = 1.18 \quad \text{and}$$

$$\frac{\kappa_{0,\mathrm{N117}}}{\kappa_{0,\mathrm{N115}}} = 1.07. \tag{A.3}$$

In the case of the Dow membrane at 368 K, it was assumed that $\kappa_0$ is about 80% higher than the conductivity of N117 under the same conditions [5].

## References


[1] S.C. Yang, M.B. Cutlip, P. Stonehart, Electrochim. Acta 35 (1990) 869.
[2] M.B. Cutlip, S.C. Yang, P. Stonehart, Electrochim. Acta 36 (1991) 547.
[3] T.E. Sringer, T.A. Zawodzinski, S. Gottesfeld, J. Electrochem. Soc. 138 (1991) 2334.
[4] D.M. Bernardi, M.W. Verbrugge, AIChE J. 37 (1991) 1151.
[5] D.M. Bernardi, M.W. Verbrugge, J. Electrochem. Soc. 139 (1992) 2477.
[6] T.F. Fuller, J. Newman, J. Electrochem. Soc. 140 (1993) 1219.
[7] T.V. Nguyen, R.E. White, J. Electrochem. Soc. 140 (1993) 2178.
[8] K. Broka, P. Ekdunge, J. Appl. Electrochem. 27 (1997) 281.
[9] G. Murgia, L. Pisani, M. Valentini, B.D. 'Aguanno, J. Electrochem. Soc. 149 (2002) A31.
[10] V. Gurau, H.T. Liu, S. Kakac, AIChE J. 44 (1998) 2410.
[11] Z.H. Wang, C.Y. Wang, K.S. Chen, J. Power Sources 94 (2001) 40.
[12] L. You, H. Liu, Int. J. Heat Mass Transfer 45 (2002) 2277.
[13] J.H. Lee, T.R. Lalk, A.J. Appleby, J. Power Sources 70 (1998) 258.
[14] G. Maggio, V. Recupero, C. Mantegazza, J. Power Sources 62 (1996) 167.
[15] D. Chu, J. Rongzhong, J. Power Sources 83 (1999) 128.
[16] J. Baschuk, X. Li, Int. J. Energy Res. 28 (2004) 697.
[17] S.J. Paddison, First principles modeling of sulfonic acid based ionomer membranes, in: W. Vielstich, H.A. Gasteiger, A. Lamm (Eds.), Handbook of Fuel Cells, vol. 3, Wiley, England, 2003, pp. 396–411.
[18] J. Kim, S.-M. Lee, S. Srinivasan, C.E. Chamberlain, J. Electrochem. Soc. 142 (1995) 2670.
[19] J.C. Amphlett, R.M. Baumert, R.F. Mann, B.A. Peppley, P.R. Roberge, T.J. Harris, J. Electrochem. Soc. 142 (1995) 1.
[20] T. Szirtes, Applied Dimensional Analysis and Modeling, McGraw-Hill, New York, 1998 (for the topic related to $\Psi$, see pp. 333–353).
[21] S.W. Churchill, Ind. Eng. Chem. Res. 31 (1992) 643.
[22] J.R. Selman, AIChE Symp. Ser. 79 (1983) 101.
[23] M.S. Quraishi, T.Z. Fahidy, Can. J. Chem. Eng. 59 (1981) 563.
[24] J. Newman, W. Tiedemann, AIChE J. 21 (1975) 25.
[25] J.D. Hellums, S.W. Churchill, AIChE J. 10 (1964) 110.
[26] S.W. Churchill, R. Usagi, Ind. Eng. Chem. Res. 13 (1974) 39.
[27] S.W. Churchill, R. Usagi, AIChE J. 18 (1972) 1121.
[28] N. Ibl, Electrochim. Acta 1 (1959) 117.
[29] U. Landau, AIChE Symp. Ser. 77 (1981) 75.
[30] S.J. Paddison, J. New. Mater. Electrochem. Syst. 4 (2001) 197.
[31] F. Meier, G. Eigenberger, Electrochim. Acta 49 (2004) 1731.
[32] J.S. Newman, Electrochemical Systems, 2nd ed., Prentice-Hall, Englewood Cliffs, NJ, 1991, pp. 222–225 and 468–470.
[33] T.A. Zawodinski, M. Neeman, L.O. Sillerud, S. Gottesfeld, J. Phys. Chem. 95 (1991) 6040.
[34] F.N. Büchi, G.G. Scherer, J. Electrochem. Soc. 148 (2001) A183.
[35] S. Srinivasan, D.J. Manko, H. Koch, M. Enayetullah, A.J. Appleby, J. Power Sources 29 (1990) 367.
[36] DuPont™ Product Information on PFSA Membranes, 2004.
[37] G.A. Eisman, J. Power Sources 29 (1990) 389.
[38] M. Doyle, G. Rajendran, Perfluorinated membranes, in: W. Vielstich, A. Lamm, H.A. Gasteiger (Eds.), Handbook of Fuel Cells, vol. 3, Wiley, Chichester, England, 2003, pp. 351–396.
[39] A. Weber, R. Darling, J. Meyers, J. Newman, Mass transfer at two-phase and three-phase interfaces, in: W. Vielstich, A. Lamm, H.A. Gasteiger (Eds.), Handbook of Fuel Cells, vol. 1, Wiley, Chichester, England, 2003, p. 59.
[40] T.E. Springer, M.S. Wilson, S. Gottesfeld, J. Electrochem. Soc. 140 (1993) 3513.
[41] J.H.G. van der Stegen, J. Görtzen, J.A.M. Kuipers, J.A. Hogendoorn, G.F. Versteeg, J. Membrane Sci. 183 (2001) 61.
[42] J. Divisek, M. Eikerling, V. Mazin, H. Schmitz, Yu.M. Volfkovich, J. Electrochem. Soc. 145 (1998) 2677.
[43] M.W. Verbrugge, R.F. Hill, J. Electrochem. Soc. 137 (1990) 3770.
[44] Yu M. Eikerling, I. Kharkats, A.A. Kornyshev, Yu M. Volfkovitch, J. Electrochem. Soc. 145 (1998) 2684.
[45] R.B. Bird, W.E. Stewart, E.N. Lightfoot, Transport Phenomena, 2nd ed., Wiley, 2002, p. 555.
[46] M.L. Perry, J. Newman, E.J. Cairns, J. Electrochem. Soc. 145 (1998) 5.
[47] L.G. Austin, Trans. Faraday Soc. 60 (1964) 1319.
[48] R. Connell, MASc Thesis, Department of Mechanical Engineering, University of British Columbia, 2005.